Computer Methods in Applied Mechanics and Engineering 453 (2026) 118797

Contents lists available at ScienceDirect

Comput. Methods Appl. Mech. Engrg.

journal homepage: www.elsevier.com/locate/cma

On the evolution of damage-induced localization in a deformable-director Cosserat continuum

Andrea Panteghini [a,*], M.B. Rubin [b]

[a] Department of Civil, Environmental, Architectural Engineering and Mathematics (DICATAM), University of Brescia, Italy
[b] Faculty of Mechanical Engineering, Technion-Israel Institute of Technology, 32000, Haifa, Israel

ARTICLE INFO

Keywords:
Damage
Deformable Cosserat model
Localization
Mesh-independent
Size-dependent
Small deformation

ABSTRACT

This paper analyzes a small-deformation, size-dependent Cosserat continuum, which in addition to the usual kinematics and balance laws admits a deformable triad of director vectors at each material point. Deformations of these directors are determined by additional director-momentum balance laws. The constitutive equations enrich elastic response with rate-independent damage that reduces the integrity of the effective resistance to distortional deformations of the material in the macro-continuum only, while leaving the stiffnesses associated with the deformable director triad unchanged. A finite element formulation for the resulting field equations is developed.

Two benchmark problems (biaxial isochoric loading and a notched plate) are analyzed to assess mesh objectivity and evolution of localization patterns. The results show that, for the examined problems, the Cosserat model with a deformable director triad predicts size-dependent yet mesh-independent shear-band initiation, width, and progression, with band thickness governed by the internal length ℓ rather than by the mesh. In contrast, the classical Cosserat baseline with a rigid director triad retains mesh sensitivity once multiple bands nucleate and evolve.

Overall, the benchmark problems examined indicate that the deformable Cosserat model has strong potential to be interpreted as a physically motivated continuum description of localized regions, rather than solely as a numerical regularization device.

1. Introduction

The Cosserat brothers [1] introduced the notion of a *generalized continuum* in which the kinematics are enriched by additional degrees of freedom at each material point, governed by additional balance equations. This approach has been used to model size effects and internal length scales.

The same philosophy of enriching the kinematics to account for microstructure was subsequently pursued in other families of generalized continua, most notably higher-order and micromorphic models. For example, the history of micromorphic theory from the original works of Eringen and Suhubi [2,3] is reviewed in [4]. Linear elastic developments of microstructural and higher-order theories can be found in the works of Germain [5] and Mindlin et al. [6–8]. Also, micropolar continuum mechanics with higher-order gradients and higher-order balance laws are discussed by Green and Rivlin [9] and by Truesdell and Toupin [10, Section 205].

Strain localization makes boundary value problems ill-posed and leads to mesh dependence. Such localization often arises as a consequence of softening phenomena due to plasticity, damage, or geometric effects. A typical manifestation is the formation of shear bands. A classical motivation for Cosserat continua with a rigid director triad, here referred to as the *rigid Cosserat model*, has been the

* Corresponding author.
E-mail addresses: andrea.panteghini@unibs.it (A. Panteghini), mbrubin@tx.technion.ac.il (M.B. Rubin).

https://doi.org/10.1016/j.cma.2026.118797
Received 10 October 2025; Received in revised form 8 January 2026; Accepted 2 February 2026
Available online 14 February 2026

physical modeling of shear bands. Pioneering contributions by Vardoulakis and co-workers and subsequent studies [11–16] showed that the rigid Cosserat model introduces an intrinsic length that mitigates mesh dependence by giving shear bands a finite thickness. The rigid Cosserat model has also been widely applied in computational analyses, including two-dimensional and three-dimensional simulations [17–19], as well as benchmark studies such as the biaxial test, where mesh-objective results can be recovered for a single shear band [20]. Practical applications have further corroborated its relevance, ranging from adiabatic shear bands in metals [21] to soil–structure interfaces [22]. However, this regularization is only partial: while rigid Cosserat formulations can alleviate the ill-posedness and yield objective results in simple settings with a single localization, they do not fully remove mesh dependence when multiple shear bands nucleate and evolve sequentially. This limitation is central to the motivation of the present work.

Building on this line of research, Rubin [23,24] recently proposed a three-dimensional Cosserat continuum enriched by a *deformable director triad* at each material point, here referred to as the *deformable Cosserat model*. This can be seen as a natural generalization of Cosserat structural theories for shells, rods, and points [25–30], where additional directors reduce the number of spatial variables while retaining microstructural effects.

The deformable director triad introduces nine additional degrees of freedom at each material point, similar to the nine degrees of freedom associated with the generic second-order tensor in micromorphic theory. An essential difference between these two approaches is that the large-deformation deformable Cosserat model in [23] uses an Eulerian formulation of constitutive equations based on internal state variables in the sense of Onat [31], thereby avoiding the arbitrariness of specifying reference and intermediate configurations as well as total and plastic deformation measures typical of Lagrangian micromorphic approaches [32,33].

This work focuses on damage-induced shear bands, chosen as a simple and convenient setting to activate localization. This choice isolates the role of the enriched kinematics, while the same framework could be naturally suited to more general strain localization mechanisms.

Several alternative regularization strategies have been developed to overcome mesh dependency. Gradient plasticity and gradient damage models introduce intrinsic length scales through higher-order deformation measures [34–38]. Viscoplastic formulations also act as regularization tools by introducing an effective length scale [39]. Nonlocal formulations based on spatial averaging were pioneered by Bažant and co-workers [40,41]. Phase-field approaches [42–44] have become increasingly popular, introducing an auxiliary field variable that regularizes damage and fracture processes. Recent extensions of phase-field formulations address more general damage and fracture processes [45], while comprehensive reviews of nonlocal plasticity and damage can be found in [46, 47]. In addition, dissipation-based gradient approaches have recently been proposed that predict mesh-independent localization profiles together with consistent energy dissipation under strong softening [48], although the assessment of their robustness in evolving localization scenarios remains an open issue. Despite their effectiveness, these approaches are often designed primarily as mathematical regularization tools.

Forest [49] discussed a micromorphic approach related to the full micromorphic theory originally proposed in [2,3], providing a generalized framework for enriched kinematics and internal length effects. Within this micromorphic framework, gradient-enhanced formulations have been proposed to model anisotropic ductile damage [50], with subsequent extensions introducing additional inertial or dynamic effects associated with internal variables [51]. In addition, it is noted that the theory and numerics of ductile micropolar models for finite deformations were considered in [52,53], where localization phenomena were explicitly investigated.

It is important to note that not all gradient or nonlocal formulations guarantee mesh-objectivity. As observed by Aravas and co-workers [54], models that include gradients of internal variables directly in the constitutive equations tend to remain elliptic at realistic stress levels, while formulations that define nonlocal variables through auxiliary Helmholtz-type problems may still lose ellipticity depending on the nonlocal hardening modulus. This highlights that the effectiveness of gradient or nonlocal regularizations depends strongly on their specific structure. Similarly, even rigid Cosserat models do not fully remove mesh sensitivity. As emphasized by Guo et al. [55], objectivity can be recovered in benchmark problems involving a single shear band under fixed loading, but sequential nucleation and interaction of multiple bands remain challenging and can reintroduce mesh dependence. These observations provide the motivation for exploring enriched frameworks.

Within the context of small deformations of the rigid Cosserat model, it is noted that: Tang et al. [56] developed an elastoplastic model considering strength anisotropy and its application to the analysis of slope stability; de Borst et al. [57] analyzed the advantages of the rigid Cosserat model for regularization of shear banding in non-associated plasticity; and Tejchman [58] considered the effect of fluctuation of the current void ratio on shear zone formation in granular bodies within micro-polar hypoplasticity. Moreover, Duretz et al. [59] presented a comparison of plasticity regularization approaches for Geodynamic modeling which included: viscoplasticity, gradient plasticity and a rigid Cosserat model. For the benchmark problems studied in [59], it was concluded that the rigid Cosserat model predicted more stable shear banding patterns and strength estimates than the other two regularization approaches. However, it was also stated there that "*…use of a Cosserat continuum is only effective for shear localization, since the rotations are mobilized only in mode-II*". Removing this limitation is central to the motivation of the present work.

Recently, Rubin [23,24] proposed a three-dimensional Cosserat continuum enriched by a *deformable director triad* at each material point, here referred to as the *deformable Cosserat model*. The micromorphic theory and the deformable Cosserat model are conceived to describe length-dependent material response, rather than to act as explicit regularization tools for localization phenomena, as in phase-field approaches. The main objective of this work is to examine the ability of the deformable Cosserat model to predict length-dependent, mesh-independent evolution of localized regions, thereby overcoming the limitations identified in the rigid Cosserat and gradient-based formulations. With this objective in mind, attention is restricted to the small-deformation elastic-damage setting, which represents the minimal framework required to trigger localization while keeping the constitutive structure as transparent as possible. Specifically, softening is introduced through an integrity function $\xi(\lambda)$ that monotonically decreases with a scalar damage variable λ, evolving in a rate-independent manner and driven by the equivalent distortional strain rate. This formulation reduces

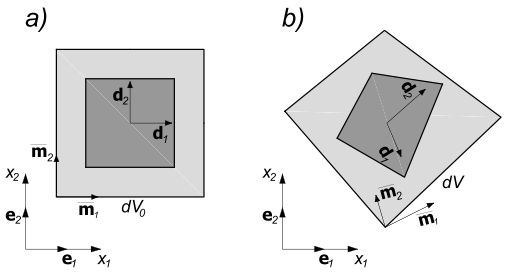

Fig. 1. A two-dimensional representation of the distortional microstructural and director vectors in a: (a) zero-stress RLS and (b) a deformed state.

the effective shear modulus of the underlying material, called the macro-continuum, while leaving the stiffnesses of the Cosserat contributions unaffected. As a result, the model mimics the macroscopic loss of stiffness due to damage while preserving the distinctive microstructural degrees of freedom. In contrast to the large-deformation thermomechanical formulation [23], this simplified setting avoids additional complexities associated with elastoplastic coupling while retaining the key features that distinguish the deformable Cosserat model from the rigid one. This highlights the specific role of the deformable directors in predicting the length dependence and the mesh independence of band thickness and progression. By direct comparison with rigid Cosserat predictions, the study aims to assess the robustness and convergence properties of the deformable model, emphasizing its potential as a physically based continuum theory for the objective modeling of localized regions.

2. The *deformable* Cosserat model

2.1. Small deformation kinematics and elastic measures of deformation

The thermomechanical Eulerian formulation of a size-dependent elastic-inelastic deformable Cosserat continuum developed in [23] introduces elastic measures of dilatation J_e, a triad of linearly independent distortional microstructural vectors $\bar{\mathbf{m}}_i$, a triad of linearly independent deformable director vectors $\mathbf{d}_i$, the director dilatation J_d and a triad of distortional directors $\bar{\mathbf{d}}_i$.[1]

To examine a simple formulation that sheds light on the ability of the deformable Cosserat theory to model localization, attention is limited to elastic response but is generalized to allow for damage of the strain energy due to the distortional deformations of the macro-continuum. As in a simple continuum, the current position $\mathbf{x}$ of a material point relative to its position $\mathbf{X}$ in a fixed reference configuration is determined by the displacement vector $\mathbf{u}$, such that

$$\mathbf{x} = \mathbf{X} + \mathbf{u}. \tag{1}$$

For small deformations, the elastic volumetric strain ε_v is defined in terms of the elastic dilatation J_e such that

$$\varepsilon_v = J_e - 1, \quad \varepsilon_v = \mathrm{tr}(\partial \mathbf{u}/\partial \mathbf{x}). \tag{2}$$

Also, the velocity gradient $\mathbf{L}$ and the rate of deformation tensor $\mathbf{D}$ are defined by

$$\mathbf{L} = \partial \dot{\mathbf{u}}/\partial \mathbf{x}, \quad \mathbf{D} = \frac{1}{2}(\mathbf{L} + \mathbf{L}^T), \tag{3}$$

where $\dot{(\,)}$ denotes partial differentiation with respect to time.

For simplicity, all vectors and tensors are referred to a fixed orthonormal triad $\mathbf{e}_i$ with Latin indices taking the values $(i = 1, 2, 3)$. The material is assumed to be in a zero-stress Reference Lattice State (RLS) when the non-dimensional quantities satisfy the equations

$$\varepsilon_v = 0, \quad \bar{\mathbf{m}}_i = \mathbf{d}_i = \mathbf{e}_i. \tag{4}$$

Fig. 1 shows two-dimensional representations of the distortional microstructural vector triad and the director triad in a zero-stress RLS Fig. 1(a) and in a deformed state Fig. 1(b). Notice that in Fig. 1(b) the vectors $\bar{\mathbf{m}}_1$ and $\bar{\mathbf{m}}_2$ have different lengths and are not orthogonal. The same is true for the directors $\mathbf{d}_1, \mathbf{d}_2$ in the deformed state.

Let $\boldsymbol{\psi}^T \equiv \partial \mathbf{u}/\partial \mathbf{x}$. For elastic deformations $\bar{\mathbf{m}}_i$ and $\mathbf{d}_i$ in the deformed state are expressed in the forms

$$\begin{aligned} &\bar{\mathbf{m}}_i = (\mathbf{I} + \boldsymbol{\psi}'^T)\mathbf{e}_i, \\ &\mathbf{d}_i = (\mathbf{I} + \boldsymbol{\eta}^T)\mathbf{e}_i, \quad \bar{\mathbf{d}}_i = (\mathbf{I} + \boldsymbol{\eta}'^T)\mathbf{e}_i, \\ &\varepsilon_{\mathrm{dir}} = \mathrm{tr}(\boldsymbol{\eta}), \end{aligned} \tag{5}$$

[1] An overbar is used to denote quantities associated with the distortional part of the kinematics. For second-order tensors, an overbar indicates a unimodular tensor obtained by removing the volumetric contribution. For director and microstructural vectors (e.g., $\bar{\mathbf{m}}_i$, $\bar{\mathbf{d}}_i$), the overbar denotes an appropriate normalization that renders the vectors independent of volumetric changes, so that they are associated only with the distortional response. This notation replaces the prime symbol used in [23]. Moreover, for any second-order tensor $\mathbf{A}$, its deviatoric (trace-free) part is $\mathbf{A}' := \mathbf{A} - \frac{1}{3}\mathrm{tr}(\mathbf{A})\,\mathbf{I}$, with $\mathbf{I}$ being the identity tensor.

where $\boldsymbol{\eta}$ is a general non-dimensional second-order tensor to be determined.

Also, the gradients of the directors are given by

$$\partial \mathbf{d}_i/\partial \mathbf{x} = \mathbf{e}_i\,(\partial \boldsymbol{\eta}/\partial \mathbf{x}). \tag{6}$$

Thus, the theory has twelve independent variables

$$\{\,\mathbf{u}, \boldsymbol{\eta}\,\}, \tag{7}$$

with three components of $\mathbf{u}$ and nine components of $\boldsymbol{\eta}$.

In [23] the deviatoric part $\bar{\mathbf{B}}'_e$ of the elastic distortional deformation tensor $\bar{\mathbf{B}}_e$, the strains χ^j_i that measure differences between $\bar{\mathbf{m}}_i$ and $\bar{\mathbf{d}}_i$ and the strains χ^k_{ij} related to components of the director gradients are given by

$$\begin{aligned} &\bar{\mathbf{B}}'_e = \boldsymbol{\psi}' + \boldsymbol{\psi}'^T, \quad \chi^j_i = (\boldsymbol{\psi}' - \boldsymbol{\eta}') \cdot (\mathbf{e}_i \otimes \mathbf{e}_j), \quad \chi^i_i = 0, \\ &\chi^k_{ij} = (\mathbf{e}_i \otimes \mathbf{e}_j + \mathbf{e}_j \otimes \mathbf{e}_i) \cdot (\partial \boldsymbol{\eta}/\partial \mathbf{x})\mathbf{e}_k, \end{aligned} \tag{8}$$

where $\mathbf{a} \otimes \mathbf{b}$ denotes the tensor product between two vectors $\mathbf{a}, \mathbf{b}$, $\mathbf{A} \cdot \mathbf{B} = \mathrm{tr}(\mathbf{A}\mathbf{B}^{\mathrm{T}})$ denotes the inner product between two second-order tensors $\mathbf{A}, \mathbf{B}$, and the usual summation convention is implied for repeated indices. Moreover, it is noted that $\chi^k_{ji} = \chi^k_{ij}$ and for later reference it can be shown that

$$\begin{aligned} &\dot{\varepsilon}_v = \mathrm{tr}(\mathbf{D}), \quad \bar{\mathbf{B}}'_e \cdot \dot{\bar{\mathbf{B}}}'_e = 2(\boldsymbol{\psi}' + \boldsymbol{\psi}'^T) \cdot \mathbf{L}, \quad \dot{\varepsilon}_{\mathrm{dir}} = \mathrm{tr}(\dot{\boldsymbol{\eta}}), \\ &\chi^j_i \chi^j_i = (\boldsymbol{\psi}' - \boldsymbol{\eta}') \cdot (\boldsymbol{\psi}' - \boldsymbol{\eta}'), \quad \chi^j_i \dot{\chi}^j_i = (\boldsymbol{\psi}'^T - \boldsymbol{\eta}'^T) \cdot (\mathbf{L} - \boldsymbol{\eta}^T), \\ &\chi^k_{ij} \dot{\chi}^k_{ij} = 2\chi^k_{ij}(\mathbf{e}_i \otimes \mathbf{e}_j + \mathbf{e}_j \otimes \mathbf{e}_i) \cdot (\partial \dot{\boldsymbol{\eta}}/\partial \mathbf{x})\mathbf{e}_k. \end{aligned} \tag{9}$$

2.2. Balance laws, boundary conditions and initial conditions

From [23] the small deformation conservation of mass, balance of linear momentum and balances of director momentum can be written in the forms

$$\begin{aligned} &\dot{\rho} = -\rho_z \dot{\varepsilon}_v, \\ &\rho_z \ddot{\mathbf{u}} = \rho_z \mathbf{b} + \mathrm{div}(\mathbf{T}), \\ &\rho_z y^{ij} \ddot{\mathbf{d}}_j = \rho_z \mathbf{b}^i - \mathbf{t}^i + \mathrm{div}(\mathbf{M}^i), \end{aligned} \tag{10}$$

In these equations, ρ_z is zero-stress density, ρ is the current density, $\mathbf{b}$ is the specific (i.e. per unit mass) external body force, div is the divergence operator with respect to $\mathbf{x}$, $\mathbf{T}$ is a second-order stress tensor, $y^{ij} = y^{ji}$ are constant director inertia coefficients having the dimensions $[\mathrm{m}^2]$, $\mathbf{b}^i$ are specific external director couples having the dimensions $[\mathrm{Pa} \cdot \mathrm{m}^3/\mathrm{kg}]$, $\mathbf{t}^i$ are intrinsic director couples having the dimensions of stress and $\mathbf{M}^i$ are second-order tensor director couples having the dimensions $[\mathrm{Pa} \cdot \mathrm{m}]$. Also, the balance of angular momentum requires the constitutive equations for $\mathbf{T}$ and $\mathbf{t}^i$ to satisfy the restriction

$$\left(\mathbf{T} + \mathbf{t}^i \otimes \mathbf{e}_i\right)^T = \mathbf{T} + \mathbf{t}^i \otimes \mathbf{e}_i, \tag{11}$$

for all motions.

Furthermore, the traction vector $\mathbf{t}$ and contact director couples $\boldsymbol{\mu}^i$ applied to a material surface ∂P with unit outward normal vector $\mathbf{n}$ are given by

$$\mathbf{t} = \mathbf{T}\mathbf{n}, \quad \boldsymbol{\mu}^i = \mathbf{M}^i \mathbf{n}. \tag{12}$$

Moreover, the rates of work applied to the body by the traction vector and the contact couples on the boundary ∂P are expressed as

$$\{\,\mathbf{t} \cdot \dot{\mathbf{u}}, \boldsymbol{\mu}^1 \cdot \dot{\mathbf{d}}_1, \boldsymbol{\mu}^2 \cdot \dot{\mathbf{d}}_2, \boldsymbol{\mu}^3 \cdot \dot{\mathbf{d}}_3\,\}, \tag{13}$$

so the boundary conditions specify the conjugate components of each of these pairs. In particular, one prescribes either $(\mathbf{u}, \mathbf{d}_i)$ (essential) or $(\mathbf{t}, \boldsymbol{\mu}^i)$ (natural) on complementary parts of ∂P. Moreover, initial conditions must be specified for

$$\{\,\rho, \mathbf{u}, \dot{\mathbf{u}}, \mathbf{d}_i, \dot{\mathbf{d}}_i\,\}. \tag{14}$$

2.3. Rate of material dissipation

Now, the stress $\mathbf{T}$ can be expressed in terms of the pressure p and its deviatoric part $\mathbf{T}'$ and the tensor $\mathbf{t}^i \otimes \mathbf{e}_i$ of intrinsic director couples can be written in terms of its pressure p_{dir} and its deviatoric part $\bar{\mathbf{t}}^i \otimes \mathbf{e}_i$, such that

$$\mathbf{T} = -p\mathbf{I} + \mathbf{T}', \quad \mathbf{t}^i \otimes \mathbf{e}_i = -p_{\mathrm{dir}}\mathbf{I} + \bar{\mathbf{t}}^i \otimes \mathbf{e}_i. \tag{15}$$

Then, the rate of material dissipation $\mathcal{D}$ for the Cosserat continuum can be written in the form

$$\begin{aligned} &\mathcal{D} = \mathcal{P} - \rho_z \dot{\Sigma} \geq 0, \quad \mathcal{P} = \mathcal{P}_p + \mathcal{P}_d, \quad \mathcal{P}_p = -p\,\mathrm{tr}(\mathbf{D}) - p_{\mathrm{dir}}\,\mathrm{tr}(\dot{\boldsymbol{\eta}}), \\ &\mathcal{P}_d = \mathbf{T}' \cdot \mathbf{L} + \left(\bar{\mathbf{t}}^i \otimes \mathbf{e}_i\right) \cdot \dot{\boldsymbol{\eta}}^T + \mathbf{M}^i \cdot [\mathbf{e}_i(\partial \dot{\boldsymbol{\eta}}/\partial \mathbf{x})], \end{aligned} \tag{16}$$

where the mechanical power $\mathcal{P}$ is separated into a part $\mathcal{P}_p$ due to the pressures p, p_{dir} and its distortional part $\mathcal{P}_d$ due to the deviatoric stress $\mathbf{T}'$, the deviatoric intrinsic director couples tensor $\bar{\mathbf{t}}^i \otimes \mathbf{e}_i$, and the second-order director couples $\mathbf{M}^i$. Also, Σ is the specific strain energy function to be specified.

2.4. Constitutive equations for a damaging elastic material

In [23] the macro-continuum experiences plasticity, the elastic strain χ_j^i measures elastic deformations of the distortional directors $\bar{\mathbf{d}}_i$ relative to the plastically deforming microstructural vectors $\bar{\mathbf{m}}^i$. Also, the elastic strain χ_{ij}^k is defined by components of the director gradients $\partial \mathbf{d}_i/\partial \mathbf{x}$ relative to $\bar{\mathbf{m}}^i$. Therefore, plasticity with decreasing yield strength reduces the resistance to distortion of the macro-continuum but does not modify the elastic resistance of the $\mathbf{d}_i$ relative to $\bar{\mathbf{m}}_i$. To simulate this effect for a damaging elastic material the strain energy function Σ is specified by

$$\begin{aligned}
&\rho_z\Sigma = \frac{1}{2}G\big(k_v\varepsilon_v^2 + k_1{\varepsilon_{\rm dir}}^2\big) + \xi(\lambda)\rho_z\Sigma_d + \frac{1}{2}G\big[k_2(\boldsymbol{\psi}' - \boldsymbol{\eta}')\cdot(\boldsymbol{\psi}' - \boldsymbol{\eta}') + \ell^2\chi_{ij}^k\chi_{ij}^k\big],\\
&\rho_z\Sigma_d = \frac{1}{4}G(\boldsymbol{\psi}' + \boldsymbol{\psi}'^T)\cdot(\boldsymbol{\psi}' + \boldsymbol{\psi}'^T),
\end{aligned} \tag{17}$$

where $\rho_z\Sigma_d$ is the distortional strain energy of the macro-continuum, G is the shear modulus and k_v can be expressed in terms of Poisson's ratio ν by

$$k_v = \frac{2(1+\nu)}{3(1-2\nu)}, \tag{18}$$

to obtain the bulk modulus k_vG of the macro-continuum. Also, $k_1 \geq 0$ is a non-dimensional constant that controls the bulk modulus of the directors, $k_2 \geq 0$ is a non-dimensional constant that controls the distortional strength of the director triad, ℓ is a characteristic material length and ξ is an integrity function having the properties

$$\xi(\lambda) > 0, \quad \xi(0) = 1, \quad \frac{\mathrm{d}\xi}{\mathrm{d}\lambda} \leq 0. \tag{19}$$

Also, λ is a damage parameter determined by the rate-independent evolution equation

$$\dot{\lambda} = \sqrt{\frac{2}{3}\mathbf{D}'\cdot\mathbf{D}'}. \tag{20}$$

This increase in the damage parameter λ causes a decrease in the integrity function ξ which reduces the effective strength to distortional deformations of the macro-continuum but does not reduce the resistance to deformations of the directors. This model for damage mimics plastic softening in the more general elastic-plastic model in [23], with plasticity only influencing the microstructural vectors $\bar{\mathbf{m}}_i$. This simple damage model is used to show that the deformable Cosserat model can model localization.

Next, the constitutive equations are specified by

$$\begin{aligned}
&p = -Gk_v\varepsilon_v, \quad p_{\rm dir} = -Gk_1\varepsilon_{\rm dir},\\
&\mathbf{T}' = G\big[\xi(\boldsymbol{\psi}' + \boldsymbol{\psi}'^T) + k_2(\boldsymbol{\psi}'^T - \boldsymbol{\eta}'^T)\big],\\
&\mathbf{t}^i = -p_{\rm dir}\mathbf{e}_i - Gk_2(\boldsymbol{\psi}'^T - \boldsymbol{\eta}'^T),\\
&\mathbf{M}^i = 2G\ell^2\chi_{ij}^k(\mathbf{e}_j\otimes\mathbf{e}_k),
\end{aligned} \tag{21}$$

which satisfy the balance of angular momentum (11). Then, using the rates (9) and the strain energy (17), the rate of material dissipation (16) requires

$$\mathcal{D} = -\dot{\xi}\rho_z\Sigma_d \geq 0\,. \tag{22}$$

which is automatically satisfied by the restrictions (19) on the integrity function ξ.

It should be noted that, in the absence of external director couples $\mathbf{b}^i$ and director inertia y^{ij}, setting $\ell = 0$ causes the present model to reduce to the standard Cauchy continuum. Indeed, the condition $\ell = 0$ implies $\mathbf{M}^i = \mathbf{0}$. Under these conditions, the balance of director momentum (10) yields $\mathbf{t}^i = \mathbf{0}$, which, through the constitutive Eq. (21), implies that the stress tensor $\mathbf{T}$ recovers the standard symmetric form of the Cauchy stress.

2.5. Component forms of the equations

For the case when the RLS is characterized by a fixed orthonormal triad $\bar{\mathbf{m}}_i = \bar{\mathbf{d}}_i = \mathbf{e}_i$, the kinematics, constitutive equations and external assigned forces and director couples are given by

$$\begin{aligned}
&\mathbf{x} = x_i\mathbf{e}_i, \quad \mathbf{u} = u_i\mathbf{e}_i, \quad \boldsymbol{\psi} = \psi_{ij}\mathbf{e}_i\otimes\mathbf{e}_j, \quad \psi_{ij} = u_{j,i}, \quad \varepsilon_v = \psi_{mm},\\
&\mathbf{d}_i = \mathbf{e}_i + \eta_{ij}\mathbf{e}_j, \quad \boldsymbol{\eta} = \eta_{ij}\mathbf{e}_i\otimes\mathbf{e}_j, \quad \varepsilon_{\rm dir} = \eta_{mm}, \quad \chi_{ij}^k = (\eta_{ij} + \eta_{ji})_{,k},\\
&\mathbf{T} = T_{ij}\mathbf{e}_i\otimes\mathbf{e}_j, \quad T_{ij} = k_vG\,\varepsilon_v\,\delta_{ij} + G\big[\xi\,(\psi'_{ij} + \psi'_{ji}) + k_2(\psi'_{ji} - \eta'_{ji})\big],\\
&\mathbf{t}^i = t_j^i\mathbf{e}_j, \quad \bar{\mathbf{t}}^i = \bar{t}_j^i\mathbf{e}_j, \quad t_j^i = Gk_1\varepsilon_{\rm dir}\,\delta_{ij} - Gk_2\big(\psi'_{ji} - \eta'_{ji}\big),\\
&\mathbf{M}^i = M_{jk}^i\mathbf{e}_j\otimes\mathbf{e}_k, \quad M_{jk}^i = 2G\,\ell^2\,(\eta_{ij} + \eta_{ji})_{,k},\\
&\mathbf{b} = b_i\mathbf{e}_i, \quad \mathbf{b}^i = b_j^i\mathbf{e}_j,
\end{aligned} \tag{23}$$

where all components are functions of (x_i, t) and a comma denotes partial differentiation with respect to x_i. Also, the strain energy function (17) and the mechanical power (16) can be rewritten in the forms

$$\begin{aligned}
&\rho_z\Sigma = \frac{1}{2}G\left[k_v(\psi_{mm})^2 + k_1(\eta_{mm})^2\right] + \xi(\lambda)\,\rho_z\Sigma_d + \frac{1}{2}G\Big[k_2(\psi'_{ij}-\eta'_{ij})(\psi'_{ij}-\eta'_{ij}) + \ell^2(\eta_{ij}+\eta_{ji})_{,k}(\eta_{ij}+\eta_{ji})_{,k}\Big],\\
&\rho_z\Sigma_d = \frac{1}{4}G\,(\psi'_{ij}+\psi'_{ji})(\psi'_{ij}+\psi'_{ji}),\\
&\mathcal{P} = \mathcal{P}_p + \mathcal{P}_d, \quad \mathcal{P}_p = -\,p\,\dot\psi_{mm} - p_{\rm dir}\,\dot\eta_{mm}, \quad \mathcal{P}_d = T'_{ij}\,\dot\psi_{ji} + \bar t^{\,i}_j\,\dot\eta_{ij} + M^i_{jk}\,\dot\eta_{ij,k}.
\end{aligned} \tag{24}$$

Then, the balances of linear and director momentum require

$$\rho_z\ddot u_i = \rho_z b_i + T_{ij,j}\,, \quad \rho_z y^{im}\ddot\eta_{mk} = \rho_z b^i_j - t^i_j + M^i_{jk,k}\,. \tag{25}$$

Also, the traction vector and the contact director couples are given by

$$\mathbf{t} = T_{ij}n_j\mathbf{e}_i, \quad \boldsymbol{\mu}^i = M^i_{jk}n_k\mathbf{e}_j, \quad \mathbf{n} = n_i\mathbf{e}_i. \tag{26}$$

For the examples considered below the integrity function is specified by

$$\xi = \frac{1}{(1+m_D\lambda)^{n_D}}, \quad m_D \geq 0, \quad n_D > 1, \tag{27}$$

where the constants m_D and n_D control the rate of damage so the restriction (22) is satisfied. The damage formulation adopted here is deliberately kept simple and phenomenological. It is not intended to represent a calibrated material damage model, but rather to provide a constitutively consistent macroscopic softening mechanism, analogous to plastic softening in the more general elastic-plastic deformable Cosserat theory of [23]. This allows strain localization to be activated while preserving the physical interpretation of the enriched Cosserat kinematics.

From (23) it can be seen that the deformable Cosserat model depends on the nine components of the director vectors η_{ij}. Specifically, T_{ij} depend on the eight components of η'_{ij} with the stiffness k_2G, t^i_j depend on all nine components of η_{ij} with the stiffnesses k_1G, k_2G and M^i_{jk} depend on the gradients of the six components of the symmetric part of η_{ij} with the length ℓ. In contrast, the rigid Cosserat model recorded in Appendix B depends on only three components of the rotation vector $\boldsymbol{\omega}$. Specifically, from (B.5) and (B.13) it can be seen that $\mathbf{T}$ depends on the $\boldsymbol{\omega}$ with the stiffness k_3G and the couple $\boldsymbol{\mu}$ depends on the gradients of $\boldsymbol{\omega}$ with the length ℓ. Thus, the deformable Cosserat model has nine extra DoFs, while the rigid Cosserat model has only three extra DoFs. Moreover, it is noted that if the director triad in the deformable Cosserat model is constrained to be rigid then η_{ij} is skew-symmetric and the director couples M^i_{jk} vanish, but T_{ij} and t^i_j retain dependence on the skew-symmetric part of η_{ij}. This means that when the deformable director triad in the deformable Cosserat model is constrained to be rigid, the small deformation theory does not reduce to that of the rigid Cosserat model. This is because the strain measures are defined via χ^k_{ij} in [23] so that they can vanish even when $\mathbf{d}_i = \bar{\mathbf{m}}_i$ is a rigid orthonormal triad that curves in space with non-zero gradients of $\mathbf{d}_i$ (e.g., along fibers), consistently with [23].[2]

2.6. Finite element formulation

The internal virtual power $\delta W_{\rm int}$ of a continuum occupying a region P is expressed as

$$\delta W_{\rm int} = \int_P \left(T_{ij}\delta\psi_{ji} + t^i_j\delta\eta_{ij} + M^i_{jk}\delta\eta_{ij,k}\right)\mathrm{d}V, \tag{28}$$

where $\delta\boldsymbol{\alpha}$ is any kinematically admissible variation of the general field $\boldsymbol{\alpha}$ and $\mathrm{d}V$ is the element of volume.

The adopted FE discretization is isoparametric, such that the same shape functions are employed to interpolate both the reference geometry and the displacement field, i.e.

$$x_j(\boldsymbol{r}) = \sum_{k=1}^{n} N^{(k)}(\boldsymbol{r})\hat x^{(k)}_j, \quad u_j(\boldsymbol{r}) = \sum_{k=1}^{n} N^{(k)}(\boldsymbol{r})\hat u^{(k)}_j,$$

where x_j and u_j are the jth components of the coordinates and of the displacement, respectively, n is the total number of nodes, $N^{(k)}(\boldsymbol{r})$ is a standard polynomial shape function referred to the kth node, $\boldsymbol{r}$ is the vector containing the intrinsic coordinates of the parent element, and $\hat x^{(k)}_j$ and $\hat u^{(k)}_j$ are, respectively, the jth coordinate and the jth displacement component of the kth node.[3] The tensor components η_{ij} are discretized as:

$$\eta_{ij}(\boldsymbol{r}) = \sum_{k=1}^{n_\eta} N^{(k)}_\eta(\boldsymbol{r})\hat\eta^{(k)}_{ij}, \tag{29}$$

where $n_\eta \leq n$ is the number of nodes in which η_{ij} is discretized, $N^{(k)}_\eta(\boldsymbol{r})$ is a standard polynomial shape function (that may be of different order with respect to $N^{(k)}(\boldsymbol{r})$) referred to the kth node, and $\hat\eta^{(k)}_{ij}$ is the ij component of $\boldsymbol{\eta}$ at the node k.

[2] A detailed discussion of the constrained deformable Cosserat formulation and its relation to both the rigid Cosserat and classical Cauchy continua is provided in Appendix A

[3] In this work the hat symbol, $\hat{(\,)}$ denotes the nodal values of the corresponding variables.

The matrices $\mathbf{H}$ and $\mathbf{H}_\eta$, respectively containing the derivatives of the shape functions $N^{(k)}$ and $N_\eta^{(k)}$ with respect to the reference coordinate system, can be computed as

$$\mathbf{H} = \boldsymbol{J}^{-1}\mathbf{H}_p, \quad \mathbf{H}_\eta = \boldsymbol{J}^{-1}\mathbf{H}_{\eta p}, \quad \boldsymbol{J} = \mathbf{H}_p\hat{\mathbf{X}}, \tag{30}$$

where $\mathbf{H}_p$ and $\mathbf{H}_{\eta p}$ are, respectively, the matrices that contain the derivatives of the shape functions $N^{(k)}$ and $N_\eta^{(k)}$ with respect to $\boldsymbol{r}$ and $\boldsymbol{J}$ is the Jacobian matrix, and $\hat{\mathbf{X}}$ is a matrix containing the nodal coordinates.

By assuming 2D plane strain, and adopting an array notation[4] the fields $\delta\boldsymbol{\psi}$, $\delta\boldsymbol{\eta}$ and $\delta\eta_{ij,k}$ can be discretized as functions of the nodal displacements and tensor variations $\delta\hat{\mathbf{u}}$, $\delta\hat{\boldsymbol{\eta}}$ as:

$$\delta\boldsymbol{\psi} = \mathcal{T}\mathcal{A}(\mathbf{H})\delta\hat{\mathbf{u}}, \quad \delta\boldsymbol{\eta} = \mathcal{N}(\mathbf{N}_\eta)\delta\hat{\boldsymbol{\eta}}, \quad \delta\eta_{ij,k} \equiv \delta\boldsymbol{\eta}_{,k} = \mathcal{G}(\mathbf{H}_\eta)\delta\hat{\boldsymbol{\eta}}, \tag{31}$$

where $\mathcal{A}(\mathbf{H})$ is a linear function[5] that maps the components of $\mathbf{H}$ into a $5\times 2n$ matrix, $\mathcal{N}(\mathbf{N}_\eta)$ is a linear function that maps the shape functions $\mathbf{N}_\eta$ into a $5\times 4n_\eta$ matrix, $\mathcal{G}(\mathbf{N}_\eta)$ is a linear function that maps the components $\mathbf{H}_\eta$ into a $8\times 4n_\eta$ matrix, and $\mathcal{T}$ is an operator to compute the transpose of a second-order tensor in the 2D array notation, all recorded in Appendix C.

Under these assumptions, (28) can be discretized as

$$\delta W_{\text{int}} = \int_P \left[\delta\hat{\mathbf{u}}^T\mathcal{A}^T\mathbf{T} + \delta\hat{\boldsymbol{\eta}}^T\left(\mathcal{N}^T\mathbf{t} + \mathcal{G}^T\mathbf{M}\right)\right]\mathrm{d}V, \tag{32}$$

which, being valid for any kinematically admissible value of $\delta\hat{\mathbf{u}}$, $\delta\hat{\boldsymbol{\eta}}$, gives the following internal forces:

$$\mathbf{F}_u^{\text{int}} = \int_P \mathcal{A}^T\mathbf{T}\mathrm{d}V, \quad \mathbf{F}_\eta^{\text{int}} = \int_P \left(\mathcal{N}^T\mathbf{t} + \mathcal{G}^T\mathbf{M}\right)\mathrm{d}V. \tag{33}$$

The stresses can be computed using (21):

$$\begin{aligned}
\mathbf{T} &= G\,\mathcal{I}_d\left[\xi(\mathcal{A}+\mathcal{T}\mathcal{A})\hat{\mathbf{u}} + k_2\left(\mathcal{A}\hat{\mathbf{u}} - \mathcal{T}\mathcal{N}\hat{\boldsymbol{\eta}}\right)\right] + \left(k_v G\right)\mathbf{I}\left(\mathbf{I}^T\mathcal{A}\hat{\mathbf{u}}\right),\\
\mathbf{t} &= -Gk_2\mathcal{I}_d\left(\mathcal{A}\hat{\mathbf{u}} - \mathcal{T}\mathcal{N}\hat{\boldsymbol{\eta}}\right) + Gk_1\mathbf{I}\left(\mathbf{I}^T\mathcal{N}\hat{\boldsymbol{\eta}}\right),\\
\mathbf{M} &= 2\,G\ell^2\left(\mathcal{G}+\mathcal{G}_{\mathcal{T}}\right)\hat{\boldsymbol{\eta}},
\end{aligned} \tag{34}$$

where $\mathcal{I}_d$ is an operator to compute the deviatoric part of a second-order tensor in the 2D array notation, and the operator $\mathcal{G}_T(\mathbf{H}_\eta)$ is a linear function that maps the components $\mathbf{H}_\eta$ into a $8\times 4n_\eta$, all reported in the Appendix C.

Finally, by defining

$$\Delta\boldsymbol{\varepsilon}' = \frac{1}{2}\mathcal{I}_d(\mathcal{A}+\mathcal{T}\mathcal{A})\Delta\hat{\mathbf{u}}, \tag{35}$$

the actual value of the damage parameter λ can be computed at the end of the increment as:

$$\lambda = \lambda_n + \sqrt{\frac{2}{3}\Delta\boldsymbol{\varepsilon}'^T\Delta\boldsymbol{\varepsilon}'}, \tag{36}$$

where λ_n is the value of λ at the previous time increment. Once λ is computed, ξ can be obtained using (27).

[4] At the implementation level, the nonzero components of each second-order 2D tensor (symmetric or non-symmetric) are stored in a 5-component array. For instance,

$$[\mathbf{T}] = \begin{bmatrix} T_{11} & T_{12} & 0\\ T_{21} & T_{22} & 0\\ 0 & 0 & T_{33}\end{bmatrix} \rightarrow \mathbf{T} = \begin{bmatrix} T_{11}\\ T_{22}\\ T_{33}\\ T_{12}\\ T_{21}\end{bmatrix}, \quad \boldsymbol{\eta} = \begin{bmatrix} \eta_{11}\\ \eta_{22}\\ 0\\ \eta_{12}\\ \eta_{21}\end{bmatrix}.$$

Similarly, also the vectors $\mathbf{t}^i$ are stored in a single array, i.e.

$$\mathbf{t}^i = t^i_j\mathbf{e}_j \rightarrow \mathbf{t} = \begin{bmatrix} t^1_1\\ t^2_2\\ t^3_3\\ t^1_2\\ t^2_1\end{bmatrix}.$$

Moreover,

$$[\boldsymbol{\eta}]_{ij,k} \rightarrow \boldsymbol{\eta}_{,k} = \begin{bmatrix} \eta_{11,1}\\ \eta_{22,1}\\ \eta_{12,1}\\ \eta_{21,1}\\ \eta_{11,2}\\ \eta_{22,2}\\ \eta_{12,2}\\ \eta_{21,2}\end{bmatrix}, \quad [\mathbf{M}]^i_{jk} \rightarrow \mathbf{M} = \begin{bmatrix} M^1_{11}\\ M^2_{21}\\ M^1_{21}\\ M^2_{11}\\ M^1_{12}\\ M^2_{22}\\ M^1_{22}\\ M^2_{12}\end{bmatrix},$$

[5] All the FE operators are reported in Appendix C.

The FE stiffness matrix is obtained by differentiating the internal forces $\mathbf{F}_u^{\rm int}$ and $\mathbf{F}_\eta^{\rm int}$ with respect to the nodal displacements $\hat{\mathbf{u}}$ and the nodal tensor $\hat{\boldsymbol{\eta}}$, i.e.,

$$\mathbf{K} = \begin{bmatrix} \mathbf{K}_{uu} & \mathbf{K}_{u\eta} \\ \mathbf{K}_{\eta u} & \mathbf{K}_{\eta\eta} \end{bmatrix} \tag{37}$$

where:

$$\mathbf{K}_{uu} = \frac{\partial \mathbf{F}_u^{\rm int}}{\partial \hat{\mathbf{u}}} = \int_P \mathcal{A}^T \left\{ G\, \mathcal{I}_d \left[\xi(\mathcal{A}+\mathcal{T}\mathcal{A}) + k_2(\mathcal{A})\right] + \left(k_v G\right)\mathbf{I}\left(\mathbf{I}^T\mathcal{A}\right) + G\, \mathcal{I}_d\left[(\mathcal{A}+\mathcal{T}\mathcal{A})\hat{\mathbf{u}}\right]\left(\frac{\mathrm{d}\xi}{\mathrm{d}\hat{\mathbf{u}}}\right)^T \right\} \mathrm{d}V, \tag{38}$$

$$\mathbf{K}_{u\eta} = \frac{\partial \mathbf{F}_u^{\rm int}}{\partial \hat{\boldsymbol{\eta}}} = \int_P -\left(k_2\, G\right)\mathcal{A}^T\, \mathcal{I}_d\, \mathcal{T}\mathcal{N}\, \mathrm{d}V, \tag{39}$$

$$\mathbf{K}_{\eta u} = \frac{\partial \mathbf{F}_\eta^{\rm int}}{\partial \hat{\mathbf{u}}} = \int_P -\left(k_2\, G\right)\mathcal{N}^T\, \mathcal{I}_d\, \mathcal{A}\, \mathrm{d}V, \tag{40}$$

$$\mathbf{K}_{\eta\eta} = \frac{\partial \mathbf{F}_\eta^{\rm int}}{\partial \hat{\boldsymbol{\eta}}} = \int_P G\left[\mathcal{N}^T\left(k_2 \mathcal{I}_d \mathcal{T} + k_1 \mathbf{I}\mathbf{I}^T\right)\mathcal{N} + 2\ell^2 \mathcal{G}^T\left(\mathcal{G}+\mathcal{G}_{\mathcal{T}}\right)\right]\mathrm{d}V. \tag{41}$$

$$\frac{\mathrm{d}\xi}{\mathrm{d}\hat{\mathbf{u}}} = \frac{\mathrm{d}\xi}{\mathrm{d}\hat{\lambda}}\frac{\mathrm{d}\hat{\lambda}}{\mathrm{d}\hat{\mathbf{u}}} = -\sqrt{\frac{1}{6}}\frac{\xi m_D n_D}{1+\lambda}\left(\frac{(\mathcal{A}+\mathcal{T}\mathcal{A})^T\Delta\boldsymbol{\varepsilon}'}{\sqrt{\Delta\boldsymbol{\varepsilon}'^T\Delta\boldsymbol{\varepsilon}'}}\right). \tag{42}$$

3. Results

In the following examples it is of interest to compare the predictions of the deformable Cosserat model with those of the rigid Cosserat model [13,14]. The finite element formulation for the rigid Cosserat model, which has been already validated in [13,14], is recorded in Appendix B for completeness.

All computations employ isoparametric *quadratic* shape functions for the displacement field and the geometry (i.e., $n = 8$, and *linear* interpolation for the non-standard Cosserat fields (i.e., $n_\eta = 4, n_\varphi = 4$), for both the rigid and the deformable formulations. All the finite element formulations adopted here have been implemented into the commercial finite element solver Abaqus [60] using a user-element subroutines (UEL).

Numerical integration uses *reduced* integration with 2×2 Gauss points per element. Hourglass tests were performed; however, no spurious (hourglass-type) zero-energy modes were observed in any simulation, which is consistent with the use of quadratic displacement/geometry elements under the present kinematics. All simulations were run in Abaqus/Standard with the default nonlinear solver settings (automatic incrementation and default convergence controls). Unless otherwise stated, the maximum load/displacement increment was limited to 1/100 of the total prescribed step. To make consistent comparisons, the same solver settings were used for both the rigid and the deformable Cosserat formulations.

Unless otherwise stated, the Cosserat fields are left free: no Dirichlet conditions are prescribed on $\boldsymbol{\eta}$ (for the deformable Cosserat) or $\boldsymbol{\varphi}$ (for the rigid Cosserat) so the boundary couples are zero unless noted.

3.1. Plane strain simple shear: Validation of the FE formulation

To validate the numerical formulation of the Cosserat implementation, numerical results are compared with those of an analytical solution for plane strain simple shear with no damage ($m_D = 0$). Details of the analytical solution are discussed in Appendix D and summarized in (D.5). Fig. 2 shows the geometry of an infinite strip of height H that is fixed at its bottom surface with its top surface moved horizontally with a uniform displacement $\bar{u}$ and additional boundary conditions on the non-standard DoFs $\boldsymbol{\eta}$. Specifically, the following BCs have been employed on the bottom and top surfaces

$$\begin{aligned} &u_1(x_1,0) = 0, \quad u_1(x_1,H) = \bar{u} = 0.1\,H, \quad u_2(x_1,0) = 0, \quad u_2(x_1,H) = 0, \\ &\eta_{21}(x_1,0) = 0, \quad \eta_{21}(x_1,H) = \bar{\eta} = 0.1, 0.2, \end{aligned} \tag{43}$$

where x_1 is the coordinate along the strip and x_2 is the coordinate through the strip's thickness.

The FE was discussed at the beginning of the Section on results; here the strip is discretized with 381 elements. For this problem the non-zero components of various quantities are given by

$$u_1(x_1,x_2), \quad \psi'_{21} = \frac{\partial u_1}{\partial x_2}, \quad \eta_{21} = \eta'_{21}(x_1,x_2). \tag{44}$$

To simulate an infinite strip along the x_1 direction, periodic boundary conditions along a strip of width equal to B have been imposed, by setting

$$\mathbf{u}(-B/2,x_2) = \mathbf{u}(B/2,x_2), \quad \boldsymbol{\eta}(-B/2,x_2) = \boldsymbol{\eta}(B/2,x_2). \tag{45}$$

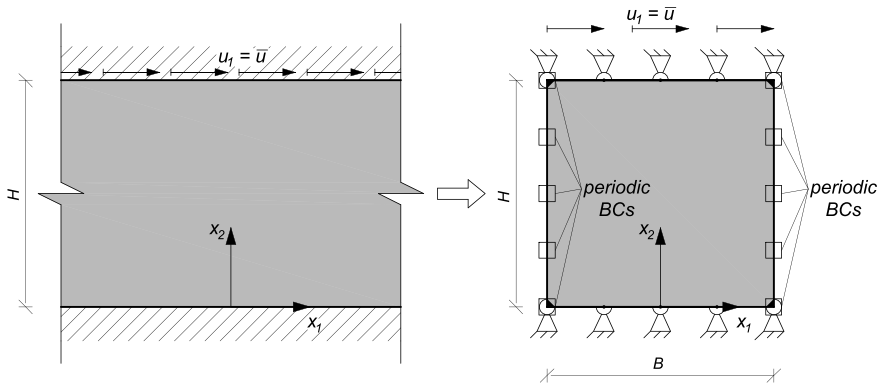

Fig. 2. Simple shear: geometry and model.

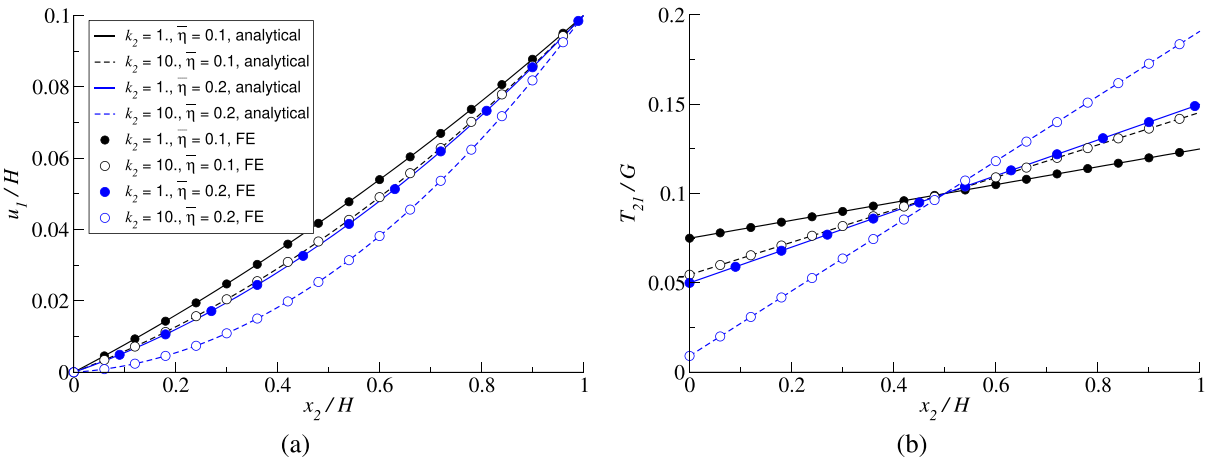

Fig. 3. Deformable Cosserat model, simple shear: comparison between the analytical and numerical results. (a) Displacement component u_1; (b) stress component T_{21}, which for this solution are independent of the material length scale ℓ.

For the simple shear solution recorded in Fig. 3 and Tables 1 and 2, $\bar{u}, k_2, \ell$ are specified by

$$\frac{\bar{u}}{H} = 0.1, \quad k_2 = 1.0, 10.0, \quad \frac{\ell}{H} = 0.1, 0.5. \tag{46}$$

Fig. 3 shows that the dependences of the displacement u_1 and the stress T_{21} on the value of k_2 for different values of $\bar{\eta}$ are identical for the analytical and numerical solutions, which validates the numerical formulation. In this family of solutions the shear stress component T_{12} is uniform (cf. Table 1), whereas T_{21} exhibits the plotted profile, with both being independent on ℓ here. Also, Table 1 records the associated values of the uniform shear stress T_{12}. From the figure and the table it is seen that increasing either k_2 or $\bar{\eta}$ increases the deviation of the fields (u_1, T_{21}) from the standard simple-shear solution.

From the analytical solution (D.5) it is noted that for $k_2 = 0$, the displacement field and the stresses reduce to those of the standard size-independent solution of simple shear for a simple continuum. Size dependence of the solution is only observed in the value of the director couples $M^1_{22} = M^2_{12}$, which are independent of k_2. Also, notice that for $\bar{\eta} = 2\bar{u}/H$ the stress T_{12} does not depend on k_2, as can be seen by the values recorded in Table 1. Moreover, T_{12} is positive for $\bar{\eta} > \bar{u} > 0$ and is negative for $\bar{u} > \bar{\eta} > 0$.

3.2. Biaxial plane strain isochoric tension–compression test

Fig. 4 shows details of the geometry for the biaxial compression and tension test under plane strain conditions, with displacement boundary conditions that would yield homogeneous isochoric deformation for a simple undamaged continuum. Due to symmetry, only one quarter of the region is simulated. Specifically, only the upper-right quadrant (region A) and the square subregion B is embedded in A at its lower-left corner are modeled. With reference to Fig. 4, the following kinematic boundary conditions are imposed on the

Table 1
Deformable Cosserat model, simple shear: comparison between the analytical and numerical results for the uniform values of the stress T_{12}, which are uninfluenced by ℓ.

k_2	$\bar{\eta}$	T_{12}/G analytical	T_{12}/G FE
1.	0.1	0.15	0.150
10.	0.1	0.6	0.600
1.	0.2	0.1	0.100
10.	0.2	0.1	0.100

Table 2
Deformable Cosserat model, simple shear: comparison between the analytical and numerical results for the values of the uniform couples $M^1_{22} = M^2_{12}$, which are uninfluenced by k_2.

ℓ/H	$\bar{\eta}$	$M^1_{22}/(GH)$ analytical	$M^1_{22}/(GH)$ FE
0.1	0.1	0.002	0.002
0.1	0.2	0.004	0.004
0.5	0.1	0.050	0.050
0.5	0.2	0.100	0.100

Table 3
Meshes for the biaxial test.

Mesh	Structured grid	Number of Elements	Number of Nodes	Characteristic Element Length	Rigid Cosserat DoFs	Deformable Cosserat DoFs
1	20×20	400	1,281	$5 \cdot 10^{-2} H$	3,003	4,326
2	40×40	1,600	4,961	$2.5 \cdot 10^{-2} H$	11,603	16,646
3	80×80	6,400	19,521	$1.25 \cdot 10^{-2} H$	45,603	65,286

upper-right quadrant:

$$\begin{aligned} \text{Bottom } (x_2 = 0): \quad & u_2(x_1, 0) = 0, \quad u_1 \text{ free}, \\ \text{Left } (x_1 = 0): \quad & u_1(0, x_2) = 0, \quad u_2 \text{ free}, \\ \text{Top } (x_2 = H): \quad & u_2(x_1, H) = \bar{u}, \quad u_1 \text{ free}, \\ \text{Right } (x_1 = H): \quad & u_1(H, x_2) = -\bar{u}, \quad u_2 \text{ free}. \end{aligned}$$

The remaining displacement components on each boundary are left free (natural conditions)

For the Cosserat fields, symmetry is enforced by specifying

$$\begin{aligned} \text{Deformable Cosserat:} \quad & \eta_{12}(x_1, 0) = \eta_{21}(x_1, 0) = 0, \quad \eta_{12}(0, x_2) = \eta_{21}(0, x_2) = 0, \\ \text{Rigid Cosserat:} \quad & \varphi_3(x_1, 0) = 0, \quad \varphi_3(0, x_2) = 0. \end{aligned}$$

All other Cosserat components are left free (i.e., on boundaries where no Dirichlet conditions are prescribed the couple-tractions vanish). The imposed displacement increases linearly during the step up to the final value $\bar{u} = 0.05\, H$.

A structured grid is intentionally adopted so that the mesh lines do not coincide with the expected shear-band trajectory, thereby minimizing alignment bias. Table 3 presents details of the three meshes used to model the biaxial test as well as the number of DoFs for both the rigid and deformable Cosserat models. Also, Table 4 records the material parameters in the regions A and B, with k_3 being the constant controlling the resistance of the rigid Cosserat model to the rotation vector (B.13). The constant ℓ controls the resistance to the gradients of the directors, relative to $\bar{\mathbf{m}}_i$, in the deformable Cosserat model and it controls the resistance to the gradient of the rotation vector in the rigid Cosserat model. In this regard, it is recalled that the linearized deformable Cosserat model has no resistance to the gradient of pure rotation of a rigid director triad. Notice from Table 4 that the constant m_D, controlling the rate of increase in damage, is 10% larger in region B than in region A, which triggers non-uniform deformation in the biaxial test.

The average vertical stress is defined as $F_2/(H\, t)$, where F_2 is the total vertical reaction force on the top boundary, H is the length of that boundary (the semi-size of region A), and t is the out-of-plane thickness (here $t = 1$ in plane strain).

Fig. 5(a) shows the average vertical stress–displacement curves predicted by the deformable Cosserat model for the three meshes described in Table 3 and for three values of ℓ/H. Fig. 5(b) shows plots of the integrity function ξ along the domain diagonal coordinate s defined to increase from the top left-hand corner of region A to the bottom right-hand corner of the region. These figures show that the results of the deformable Cosserat model converge with mesh refinement (mesh 3 being the finest), with different results

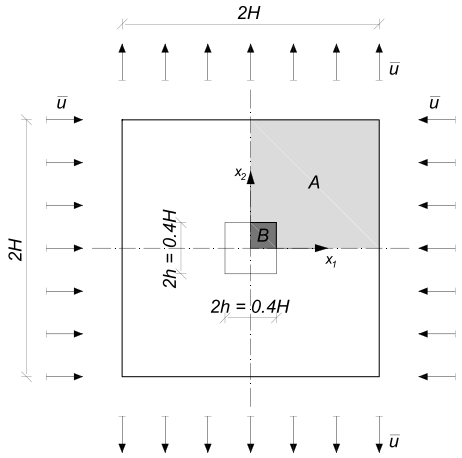

Fig. 4. Biaxial problem.

Table 4
Material parameters for the biaxial test.

Region	Material Parameters
A	$G = 50000.\,\text{MPa}$, $k_v = 1.2$, $k_1 = 0.1$, $k_2 = 0.25$, $m_D = 50.$, $n_D = 2.0$, $k_3 = 1.1$
B	$G = 50000.\,\text{MPa}$, $k_v = 1.2$, $k_1 = 0.1$, $k_2 = 0.25$, $m_D = 55.$, $n_D = 2.0$, $k_3 = 1.1$

for the different values of $r = \ell/H$. In this regard, it is emphasized that the material parameters in the deformable Cosserat model predict the evolution and shape of the shear band. Specifically, Fig. 5(b) plots the values of the integrity function along the domain diagonal at the end of the loading step ($\bar{u}/H = 0.05$), with a localization region whose extent depends on ℓ. The shear-band width can be quantified in an operational manner as the portion of the domain diagonal over which the integrity function satisfies $\xi \leq 0.2$, normalized by the diagonal length $H\sqrt{2}$. For the finest mesh, this normalized width is approximately 0.215 for $r = \ell/H = 1/200$, 0.152 for $r = 1/400$, and 0.116 for $r = 1/1000$, confirming that the thickness of the localized zone decreases monotonically with decreasing internal length.

Also, Fig. 5(c) includes plots of the *external work*, normalized by GH^2t, which accumulates the work of the reactions on all displacement-controlled boundaries (top and right). For the deformable Cosserat formulation this provides a compact global indicator of mesh-objectivity, serving instead as a global indicator of numerical consistency, in the sense that for a given value of r the corresponding curves remain close across different meshes. As an integral quantity, the external work is inherently less sensitive to local differences in the spatial structure of the solution; consequently, deviations associated with mesh dependence typically manifest themselves in local field quantities, such as damage or strain contours.

Figs. 6–8 show the evolution of contours of the integrity ξ function for different values of the load $\bar{u}/H$ and for the three different meshes and the same value of $\ell/H = 1/1000$ for the deformable Cosserat model. From these figures it can be seen that the shape of the entire shear band converges nicely with mesh refinement.

In contrast, Fig. 9 shows that the predictions of the average vertical stress–displacement curves for the rigid Cosserat model do not converge with mesh refinement and that the simulations crash for different values of the load $\bar{u}/H$. The value $r = \ell/H = 1/200$ was deliberately used in both formulations: it corresponds to the smallest value considered for the rigid Cosserat model and to the largest value considered for the deformable Cosserat formulation, enabling a direct qualitative comparison, although the influence of ℓ is different in the two models. This choice was made to assess the ability of the two formulations to regularize pronounced softening responses within a comparable numerical setting, since the rigid Cosserat model already exhibits convergence difficulties at this value, whereas the deformable formulation remains stable for substantially steeper softening branches.

Figs. 10–12 show the evolution of contours of the integrity ξ function for values of the load $\bar{u}/H$ just before each simulation crashes for the rigid Cosserat model. Each figure shows results for three different meshes. Specifically, Fig. 10 shows results for $\bar{u}/H = 0.02$, $\ell/H = 1/200$, Fig. 11 shows results for $\bar{u}/H = 0.03$, $\ell/H = 1/40$, and Fig. 12 shows results for $\bar{u}/H = 0.048$, $\ell/H = 1/20$. From these figures it can be seen that contours of the integrity ξ do not converge with mesh refinement. For the intermediate and small material lengths considered, different meshes lead to distinct nucleation paths and band orientations; therefore ξ along a fixed diagonal is not plotted and the contour sequences are used as the primary evidence of mesh sensitivity. For the rigid Cosserat formulation, external-work curves were also examined but are not reported. A divergence in the slope can indeed be observed; however, this occurs only in a very small interval immediately preceding numerical lack of convergence. Since simulations performed on different meshes terminate at different load levels due to numerical breakdown, there is no common loading range over which a meaningful comparison of the external-work curves can be carried out. As a result, the assessment of mesh objectivity is primarily based on the evolution of the internal fields, rather than on global energetic measures, which may remain deceptively similar up to numerical collapse.

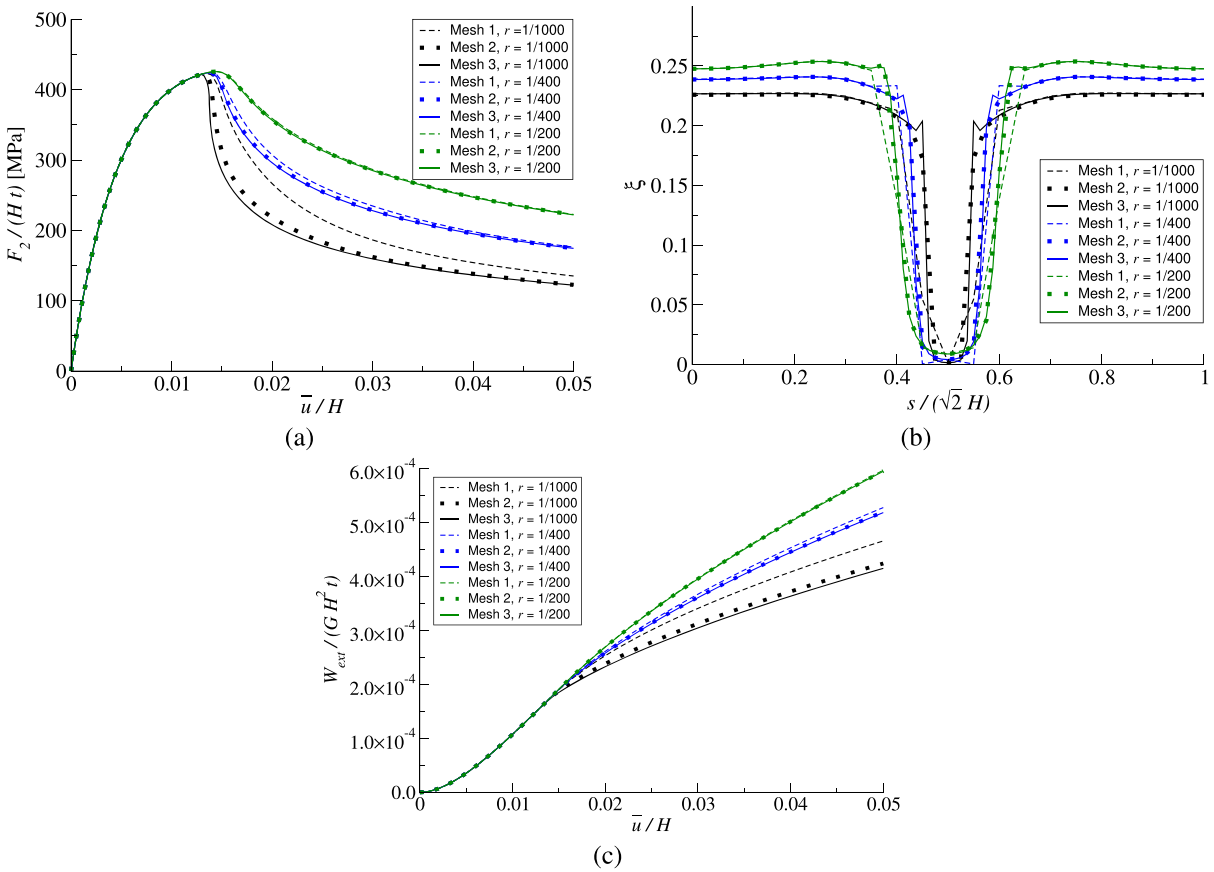

Fig. 5. Deformable Cosserat model, biaxial test. (a) Average vertical stress–displacement curves, with $\langle \sigma_{yy} \rangle = F_2/(H\,t)$. (b) Shear band shapes at the end of the loading predicted by different values of $r = \ell/H$ for different meshes. (c) Normalized external work $W_{\text{ext}} = W_{\text{ext}}/(G\,H^2\,t)$ vs. displacement for different values of $r = \ell/H$ and different meshes (plane strain with unit thickness $t = 1$).

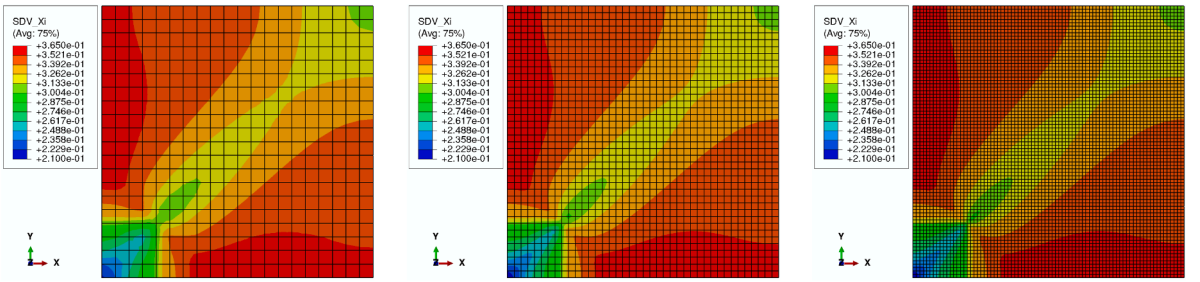

Fig. 6. Deformable Cosserat model, biaxial test. Contour plots of ξ at $\bar{u}/H = 0.0125$ for $\ell/H = 1/1000$. (a) mesh 1, (b) mesh 2, (c) mesh 3.

3.3. Notched plate test

Fig. 13 shows details of the geometry for the notched plate test and Table 5 records the values of the material parameters for this test. Due to symmetry, only one quarter of the region is simulated. With reference to Fig. 13, the following kinematic boundary conditions are imposed on the upper-right quadrant:

$$\begin{aligned} \text{Bottom } (x_2 = 0): &\quad u_2(x_1, 0) = 0, \quad u_1 \text{ free}, \\ \text{Left } (x_1 = 0): &\quad u_1(0, x_2) = 0, \quad u_2 \text{ free}, \\ \text{Top } (x_2 = H): &\quad u_2(x_1, H) = \bar{u}, \quad u_1 \text{ free}, \\ \text{Right } (x_1 = B): &\quad u_1, u_2 \text{ free (natural conditions)}. \end{aligned}$$

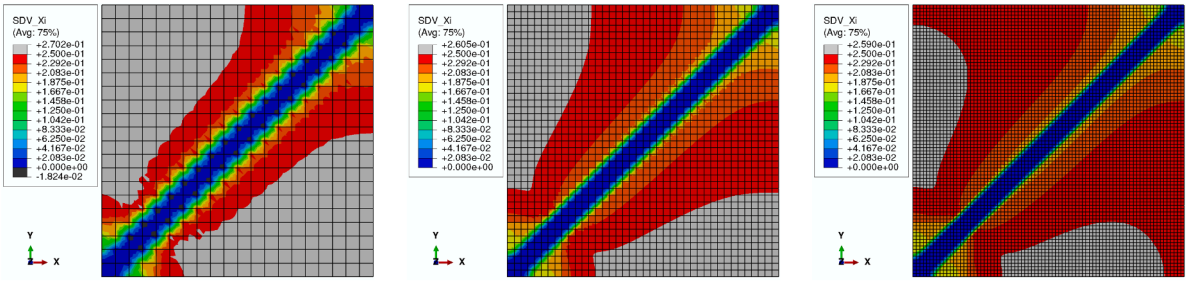

Fig. 7. Deformable Cosserat model, biaxial test: contour plots of ξ at $\bar{u}/H = 0.025$ for $\ell/H = 1/1000$. (a) mesh 1, (b) mesh 2, (c) mesh 3.

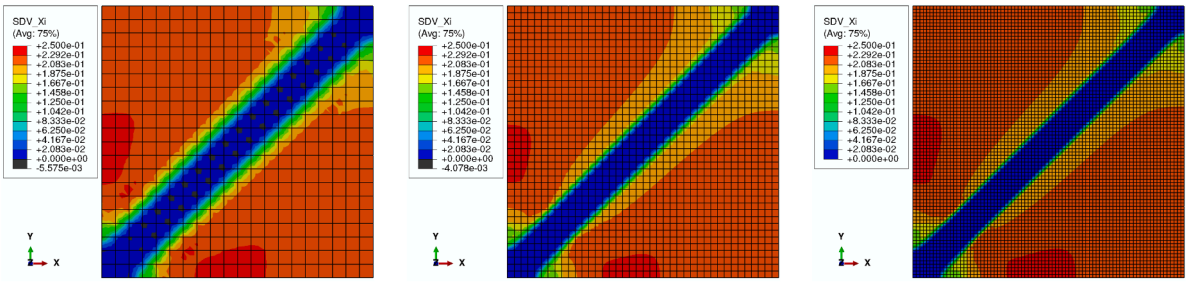

Fig. 8. Deformable Cosserat model, biaxial test: contour plots of ξ at $\bar{u}/H = 0.05$ for $\ell/H = 1/1000$. (a) mesh 1, (b) mesh 2, (c) mesh 3.

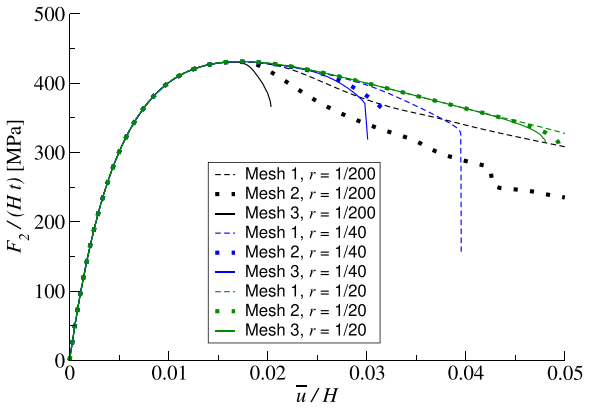

Fig. 9. Rigid Cosserat model, biaxial test. Average vertical stress–displacement curves for different values of $r = \ell/H$. The curves diverge near the last converged step for each analysis.

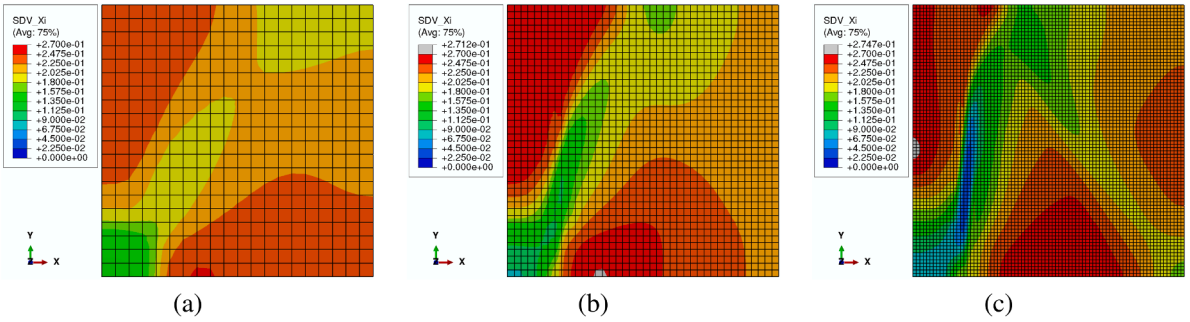

Fig. 10. Rigid Cosserat model, biaxial test: contour plots of ξ at $\bar{u}/H = 0.02$ for $\ell/H = 1/200$. (a) mesh 1, (b) mesh 2, (c) mesh 3. Different meshes produce different band localizations and orientation at this early stage, evidencing mesh sensitivity.

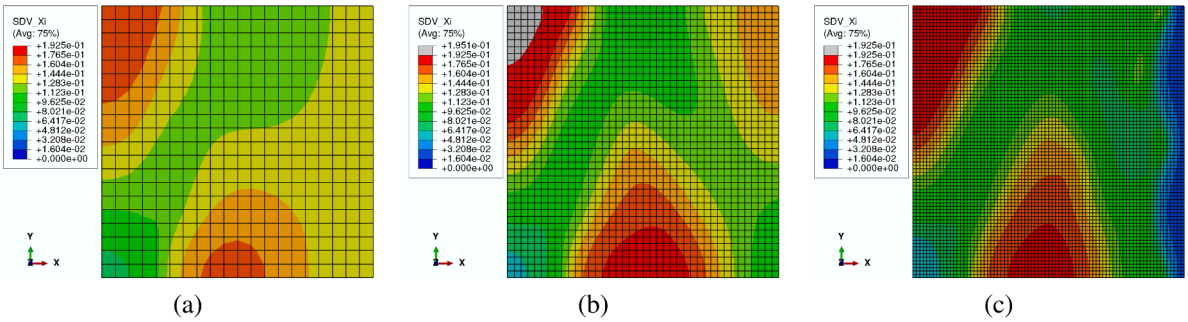

Fig. 11. Rigid Cosserat model, biaxial test: contour plots of ξ at $\bar{u}/H = 0.03$ for $\ell/H = 1/40$. (a) mesh 1, (b) mesh 2, (c) mesh 3. Mesh-dependent position and orientation differences are pronounced for this intermediate internal length.

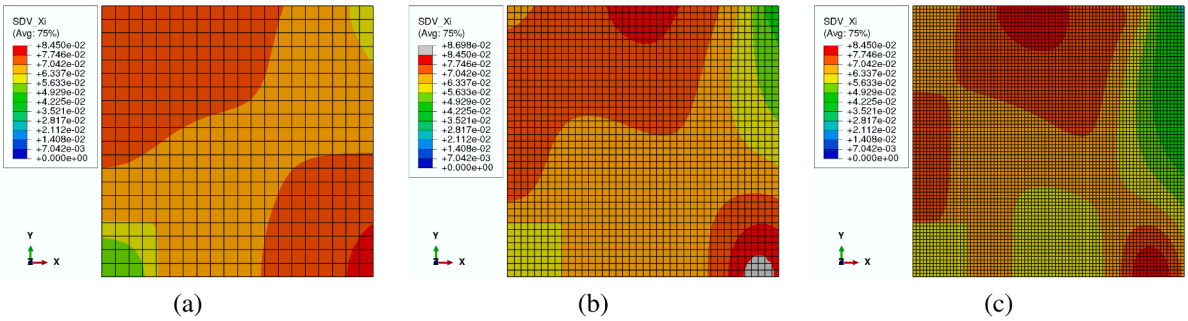

Fig. 12. Rigid Cosserat model, biaxial test: contour plots of ξ at $\bar{u}/H = 0.048$ for $\ell/H = 1/20$. (a) mesh 1, (b) mesh 2, (c) mesh 3. Comparison of the figures indicates that the band position and orientation does not converge to a unique pattern, confirming lack of mesh-objective convergence for this large internal length.

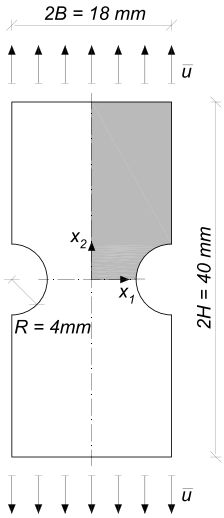

Fig. 13. Notched plate test.

The remaining displacement components on each boundary are left free (natural conditions). On all free outer edges and on the notch faces tractions and couple-tractions vanish.

For the Cosserat fields, symmetry is enforced by specifying

$$\text{Deformable Cosserat:} \quad \eta_{12}(x_1,0) = \eta_{21}(x_1,0) = 0, \quad \eta_{12}(0,x_2) = \eta_{21}(0,x_2) = 0,$$
$$\text{Rigid Cosserat:} \quad \varphi_3(x_1,0) = 0, \quad \varphi_3(0,x_2) = 0.$$

No Dirichlet conditions are imposed on the Cosserat fields along the top and right edges; where no Dirichlet is prescribed, couple-tractions are set to zero. The imposed displacement increases linearly during the step up to the final value $\bar{u} = 0.005\, H$.

Table 5
Material parameters for the notched plate test.

$G = 80769.2\,\text{MPa}$, $k_\upsilon = 2.16667$, $k_1 = 0.1$, $k_2 = 0.25$, $m_D = 807.69$, $n_D = 2.0$, $k_3 = 1.1$

Table 6
Meshes for the notched plate test.

Mesh	Number of Elements	Number of Nodes	Characteristic Element Length ℓ_e	Rigid Cosserat DoFs	Deformable Cosserat DoFs
1	503	1,616	0.360 mm	3,789	5,460
2	2,848	8,757	0.143 mm	20,469	29,334
3	12,234	37,129	$6.657 \cdot 10^{-2}$ mm	86,706	124,050
4	44,263	133,642	$3.721 \cdot 10^{-2}$ mm	311,974	446,044
5	146,931	442,370	$2.267 \cdot 10^{-2}$ mm	1,032,460	1,475,620

Table 7
Size of ℓ relative to the characteristic element length ℓ_e for the five meshes of the notched plate test.

Mesh	ℓ/H	ℓ/ℓ_e	ℓ/H	ℓ/ℓ_e	ℓ/H	ℓ/ℓ_e
1	1/2000	0.0278	1/800	0.0694	1/400	0.139
2	1/2000	0.0700	1/800	0.175	1/400	0.350
3	1/2000	0.150	1/800	0.376	1/400	0.751
4	1/2000	0.269	1/800	0.672	1/400	1.34
5	1/2000	0.441	1/800	1.10	1/400	2.21

Fig. 14 shows five meshes that were used to study convergence due to mesh refinement. They are described in Table 6. In this example the average vertical stress as $F_2/B\,t$ is plotted, where F_2 is the total vertical reaction on the driven (top) boundary, B is the length of that boundary in the simulated domain (cf. Fig. 13), and t is the out-of-plane thickness (unit thickness in plane strain).

Fig. 15(a) shows the average vertical stress–displacement curves for three meshes and three values of $r = \ell/H$, and Fig. 15(b) shows convergence of the stress–displacement curves for the smallest value $r = \ell/H = 1/2000$ and for five meshes. For both $r = \ell/H = 1/800$ and $r = \ell/H = 1/400$ the solutions are converged by mesh 3, whereas for $r = \ell/H = 1/2000$ a finer mesh is required, as seen in Fig. 15(b). For $r = \ell/H = 1/2000$, the finest meshes 4 and 5 yield nearly identical results and indicate a second softening mechanism near $\bar{u}/H \approx 0.0015$. From Fig. 15(a) it is observed that this second softening mechanism is influenced by the value of $r = \ell/H$. Table 7 records the size of ℓ relative to the characteristic element length ℓ_e for the five meshes. Convergence is obtained for $r = \ell/H = 1/800$ and 1/400 with mesh 3 and for $r = \ell/H = 1/2000$ with mesh 5, suggesting an empirical resolution criterion $\ell/\ell_e \gtrsim 1/2$.

To understand the evolution of the localization process, Figs. 16–18 show contours of the integrity function ξ for three meshes, at the same internal length $\ell/H = 1/2000$, for three load levels $\bar{u}/H = 5 \cdot 10^{-4}, 1 \cdot 10^{-3}$ and $5 \cdot 10^{-3}$. From these figures it is concluded that a shear band starts at the bottom right-hand corner of the notch and expands towards the centerline of the plate, causing the first peak in Fig. 15. The second softening mechanism is due to a second shear band that expands from the centerline of the plate toward its outer edge. Most importantly, these figures show that the predictions of the deformable Cosserat model converge to the same localized regions for each fixed value of $r = \ell/H$.

Figs. 19–21 show the evolution of converged contour plots of the integrity ξ for the deformable Cosserat model for different loads $\bar{u}/H$ and three values $r = \ell/H = 1/2000, 1/800, 1/400$. From these figures it is clear that the evolution of ξ is significantly influenced by $r = \ell/H$. Specifically, for the smallest value $r = \ell/H = 1/2000$ (largest specimen), more intricate band features are observed. Although the contour plots are nearly identical for the lowest load (Fig. 19), differences are observed at the intermediate load (Fig. 20), with the contours for the highest load (Fig. 21) being quite different across r. These figures emphasize that the deformable Cosserat model can be used to predict the localization process and is not just a numerical regularization, because the converged contours depend on the specified $r = \ell/H$. Also, from Fig. 15(a) it can be seen that the smaller specimens (i.e., larger $r = \ell/H$) tend to damage more slowly with increasing $\bar{u}/H$ than larger specimens, which is consistent with the notion that smaller specimens tend to be stronger than larger specimens.

In contrast, Fig. 22 shows that the simulations of the rigid Cosserat model for the smallest two values of $r = \ell/H$ crash and do not converge with mesh refinement. Moreover, even for the largest value of ℓ/H the predictions exhibit slow convergence. Because only the top boundary is displacement-driven (single amplitude), the external work is equal to the area under the reaction–displacement curve and is therefore omitted.

Also, the influence of k_2 was examined by considering $k_2 = 0.25, 0.50, 1.0$. Specifically, simulations were performed on the notched plate test with the finest mesh 5 and it was found that this range of k_2 does not cause a significant difference in the average force–displacement curve in Fig. 15(b) or on the localization regions in Fig. 21.

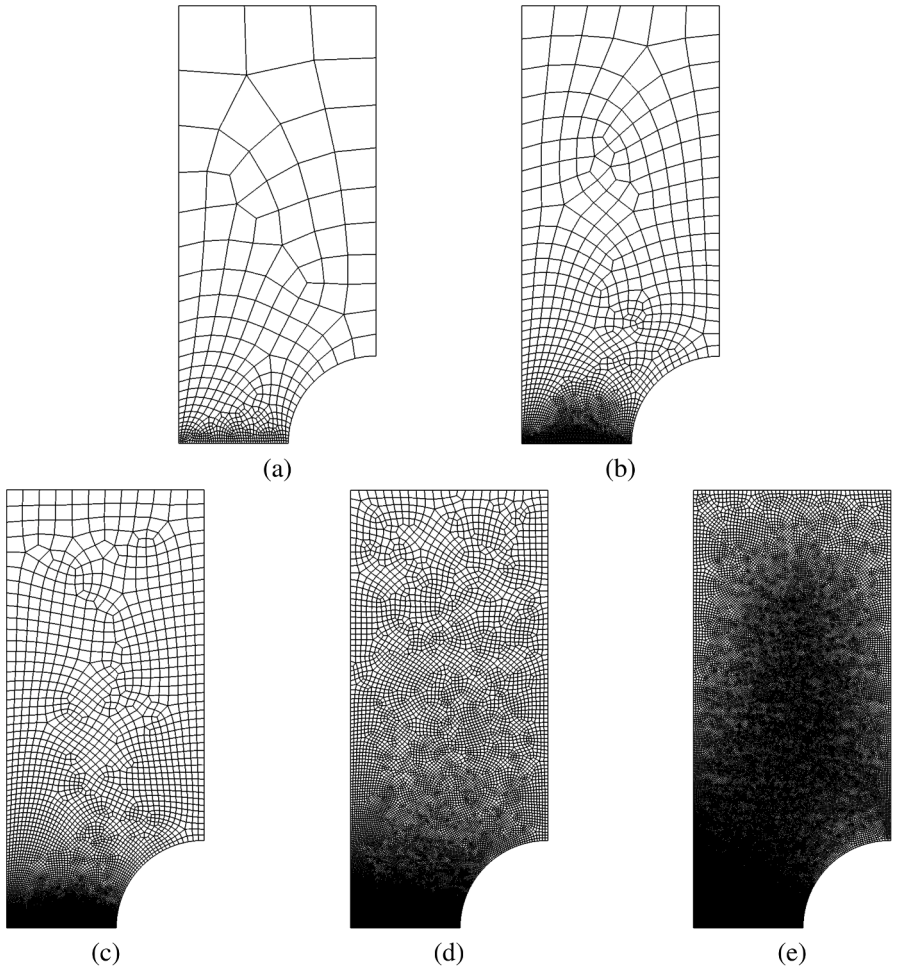

Fig. 14. Notched plate test: discretization: (a) mesh 1, (b) mesh 2, (c) mesh 3, (d) mesh 4, (e) mesh 5.

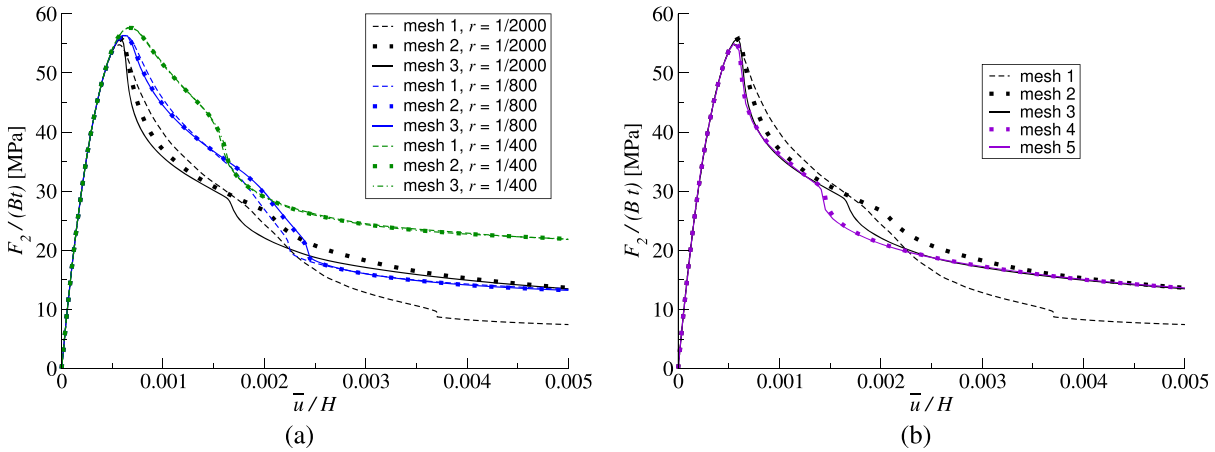

Fig. 15. Deformable Cosserat model, notched plate test. (a) Average vertical stress-displacement curves. (b) convergence study for $r = \ell / H = 1/2000$.

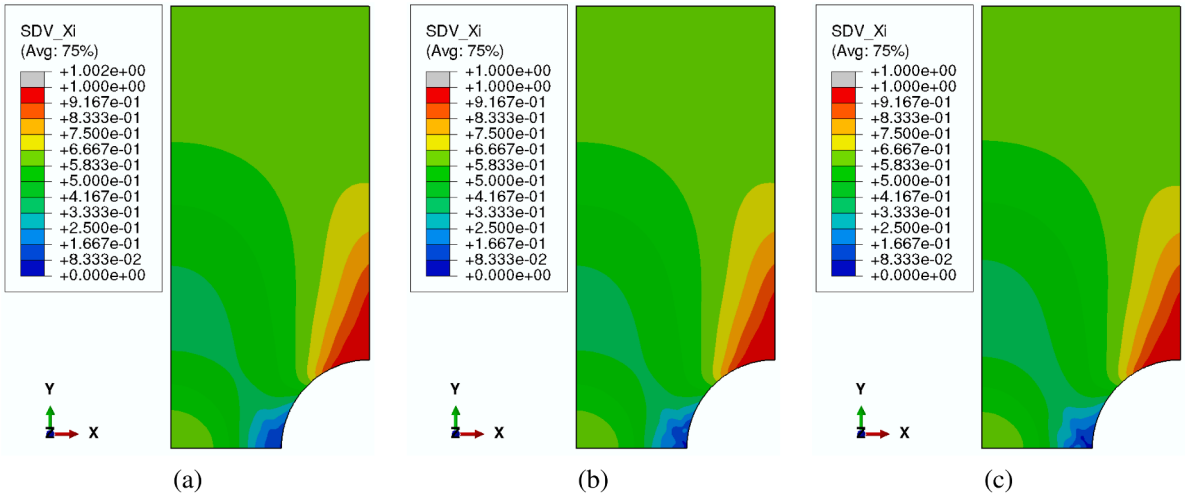

Fig. 16. Deformable Cosserat model, notched plate test: contour plots of ξ at $\bar{u}/H = 5 \cdot 10^{-4}$ for $\ell/H = 1/2000$. (a) mesh 3, (b) mesh 4, (c) mesh 5.

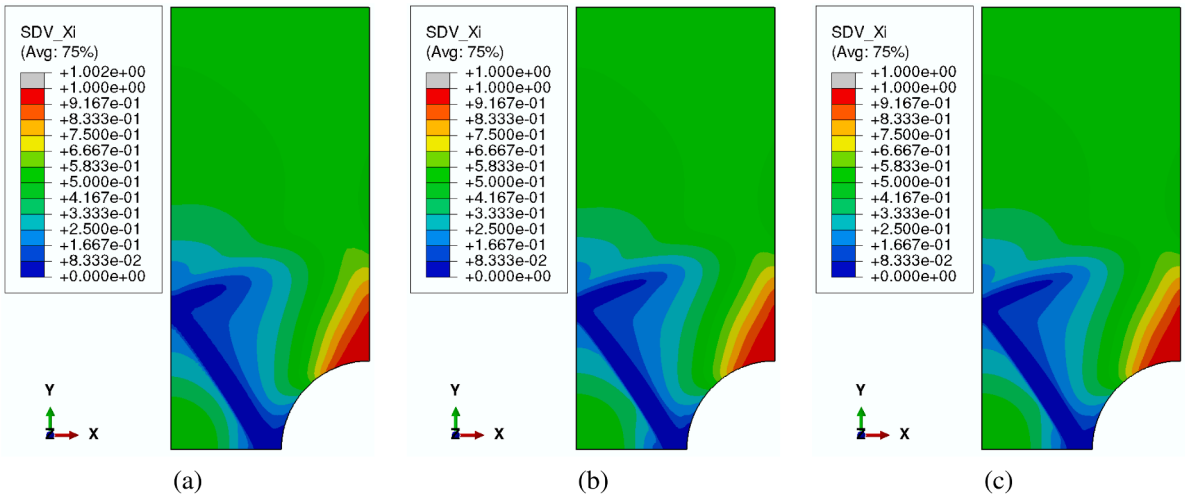

Fig. 17. Deformable Cosserat model, notched plate test: contour plots of ξ at $\bar{u}/H = 1 \cdot 10^{-3}$ for $\ell/H = 1/2000$. (a) mesh 3, (b) mesh 4, (c) mesh 5.

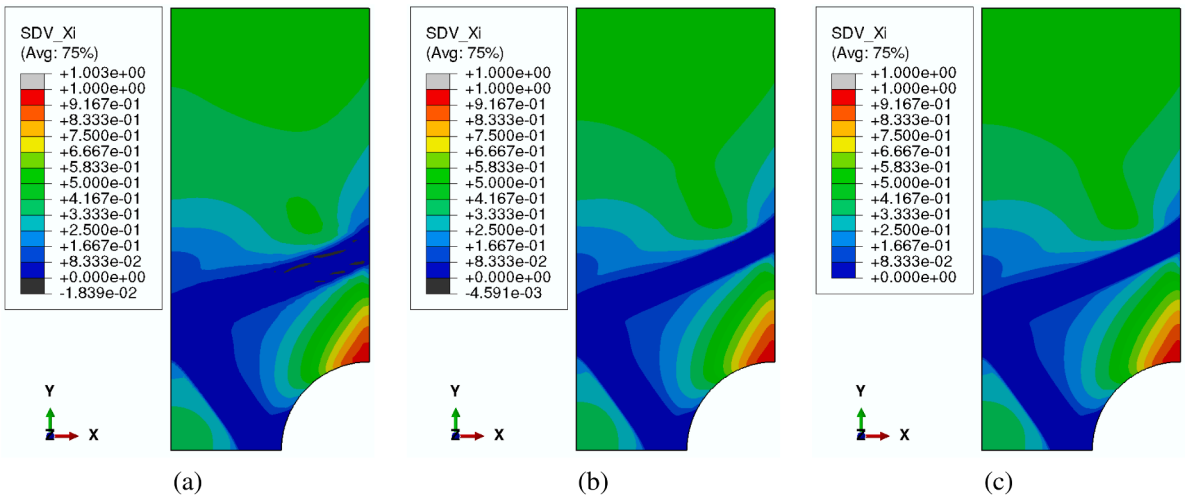

Fig. 18. Deformable Cosserat model, notched plate test: contour plots of ξ at $\bar{u}/H = 5 \cdot 10^{-3}$ for $\ell/H = 1/2000$. (a) mesh 3, (b) mesh 4, (c) mesh 5.

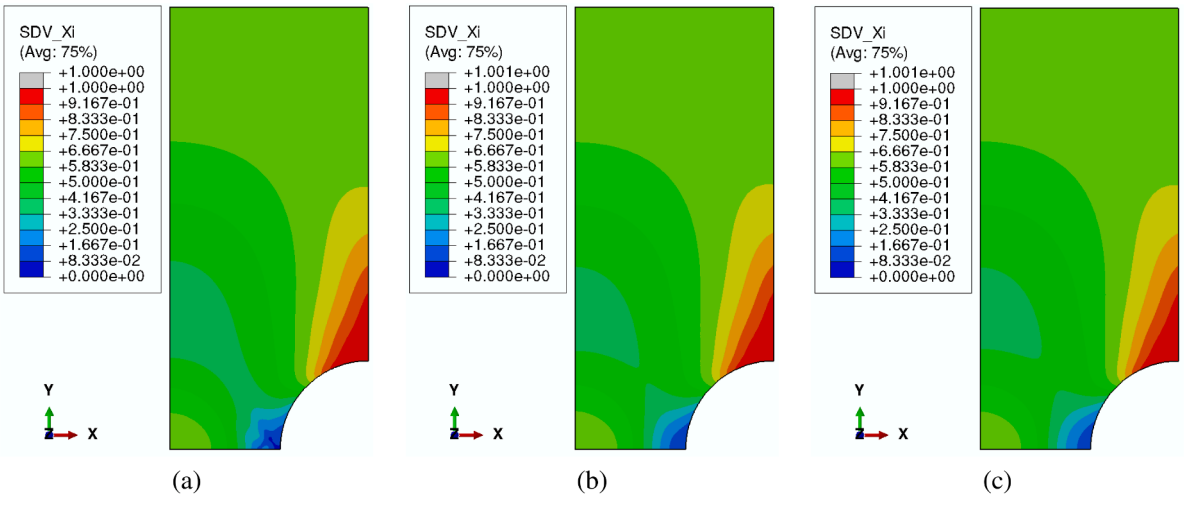

Fig. 19. Deformable Cosserat model, notched plate test: converged contour plots of ξ at $\bar{u}/H = 5 \cdot 10^{-4}$ for (a) $\ell/H = 1/2000$ (mesh 5), (b) $\ell/H = 1/800$ (mesh 3), (c) $\ell/H = 1/400$ (mesh 3).

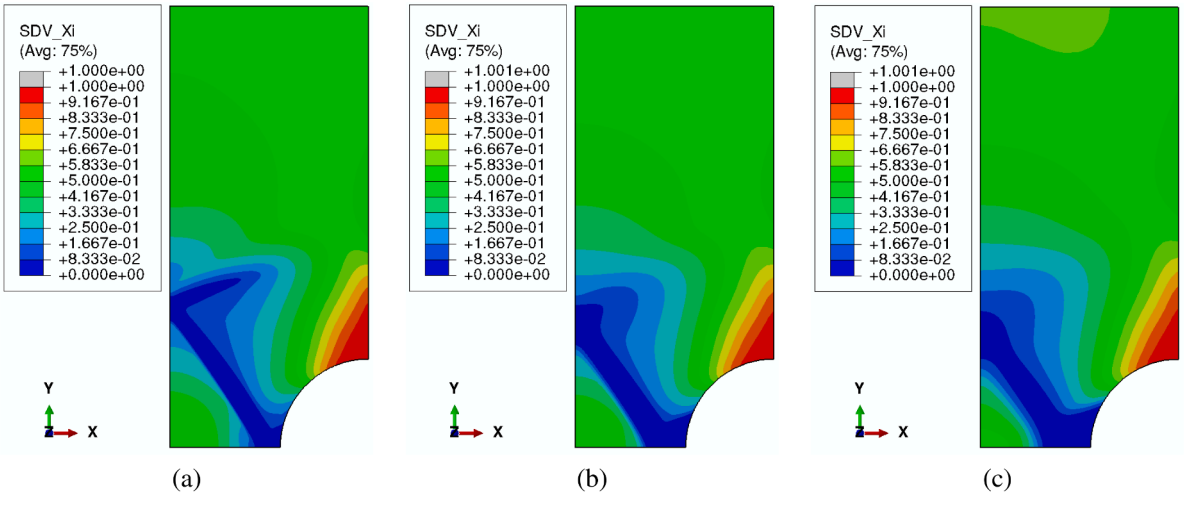

Fig. 20. Deformable Cosserat model, notched plate test: converged contour plots of ξ at $\bar{u}/H = 1 \cdot 10^{-3}$ for (a) $r = \ell/H = 1/2000$ (mesh 5), (b) $r = \ell/H = 1/800$ (mesh 3), (c) $r = \ell/H = 1/400$ mesh 3.

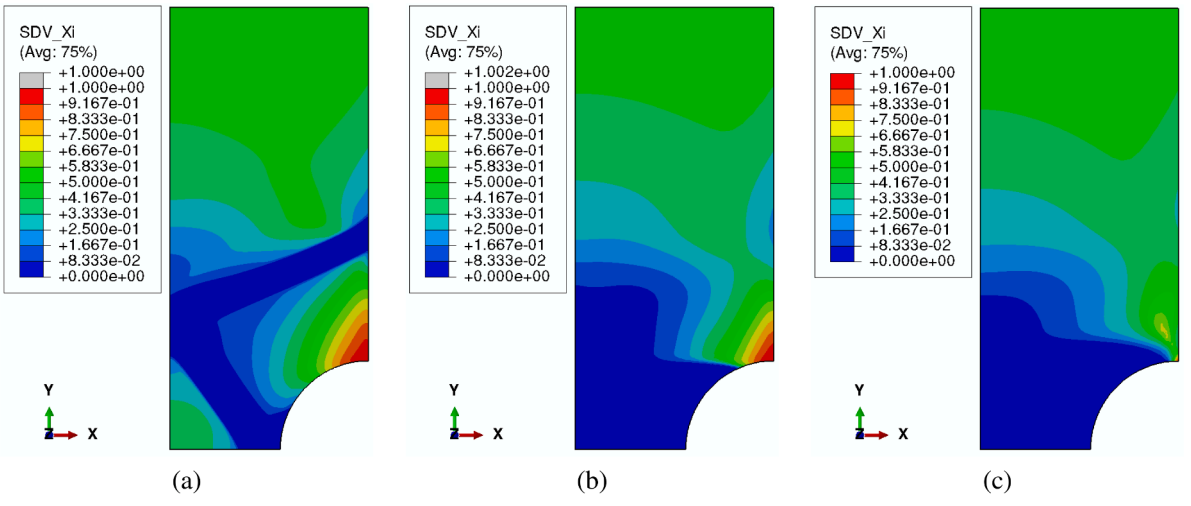

Fig. 21. Deformable Cosserat model, notched plate test: converged contour plots of ξ at $\bar{u}/H = 5 \cdot 10^{-3}$ for (a) $\ell/H = 1/2000$ (mesh 5), (b) $\ell/H = 1/800$ (mesh 3), (c) $\ell/H = 1/400$ (mesh 3).

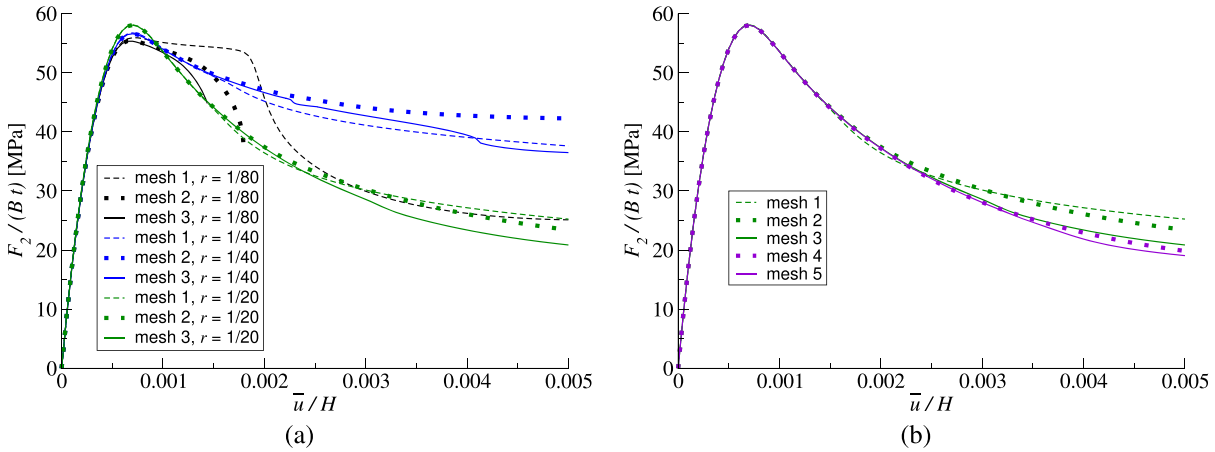

Fig. 22. Rigid Cosserat model, notched plate test. (a) Average vertical stress-displacement curves. (b) convergence study for $r = \ell/H = 1/20$.

Conclusions

A thermomechanical three-dimensional Cosserat theory was developed in [23] for anisotropic elastic-inelastic response. In this model the macro-continuum is enriched by a deformable triad of director vectors at each material point that are determined by higher-order balances of director momentum. In the present formulation, macroscopic elastic deformation is described in terms of volumetric and distortional measures regarded as internal state variables, while the microstructural response is captured by the deformations and gradients of the director triad governed by the additional balances of director momentum. In contrast, with the standard rigid Cosserat model with the macro-continuum enhanced by a rigid director triad with three degrees of freedom, the deformable Cosserat model is enhanced with nine degrees of freedom for the director triad. In the proposed small-deformation elastic-damage setting softening acts only on the macro-continuum, while director deformations remain elastic and are governed by the higher-order balances.

It is well known that damage or softening of the resistance to plastic flow can cause localization regions with high strain gradients. This typically causes mesh dependence in numerical solutions. Standard methods to regularize this localization include adding rotational degrees of freedom with the rigid Cosserat model or introducing phase-field variables to smooth the solution. The objective of this paper is to assess the ability of the deformable Cosserat model to predict the evolution of localization regions. To this end, attention is limited to the small-deformation, purely mechanical equations of this deformable Cosserat model for elastic response with softening characterized by an integrity function ξ in the strain energy (17) that reduces only the macro-continuum shear resistance. This softening mechanism initiates the development of localization regions and mimics softening that would occur due to decrease in yield strength in an elastic-inelastic model. The resulting finite-element formulation was exercised on benchmark problems to assess mesh objectivity and band evolution. Preliminary identification/sensitivity is also provided, showing how the internal length controls band thickness and pattern selection of localized regions.

Examples demonstrate that the resulting deformable Cosserat model predicts length-dependent, mesh-independent evolution of localization regions including sequential nucleation in the examined problems. Since the localization regions are influenced by the physical material parameters in the deformable Cosserat model, these results suggest that the model should not be viewed solely as a numerical regularization technique, but rather as a continuum formulation with predictive potential for the evolution of localized regions. It is conjectured that the improved robustness primarily follows from the richer micro-kinematics of the deformable director triad and its associated gradient/curvature terms, which strengthen the highest-order operator beyond the purely rotational curvature of a rigid Cosserat model. In the examples, the rigid Cosserat benchmark did not exhibit robustness comparable to that of the deformable Cosserat model once the patterns evolved, with loss of convergence and sensitivity to mesh in those settings.

Future research is needed to examine the performance of the deformable Cosserat model for more general material behavior. Specifically, future work might include the study of: elastoplastic response of geomaterials, including softening and non-associative flow rules; well-posedness/ellipticity; and a more systematic parameter identification (e.g., internal lengths and shear moduli) under triaxial/biaxial loading.

CRediT authorship contribution statement

Andrea Panteghini: Writing – review & editing, Writing – original draft, Visualization, Validation, Software, Project administration, Methodology, Investigation, Formal analysis, Data curation, Conceptualization; **M.B. Rubin:** Writing – review & editing, Writing – original draft, Validation, Methodology, Investigation, Formal analysis, Data curation, Conceptualization.

Data availability

Data will be made available on request.

Declaration of competing interest

The authors declare that they have no known competing financial interests or personal relationships that could have appeared to influence the work reported in this paper.

Acknowledgements

The authors would like to thank Prof. L. Bardella for calling our attention to some references relevant to the present work. Simulia Abaqus has been run at DICATAM - University of Brescia, under an academic license.

Appendix A. A constrained deformable Cosserat model

A rigid director triad can be obtained using the deformable Cosserat model by imposing suitable kinematic constraints on the director fields. Specifically, the rigid triad constraint is expressed as

$$\mathbf{d}_i \cdot \mathbf{d}_j = \delta_{ij}, \qquad \boldsymbol{\eta}^T = -\boldsymbol{\eta}, \tag{A.1}$$

where δ_{ij} denotes the Kronecker symbol and $\boldsymbol{\eta}$ is the skew-symmetric tensor that characterizes the angular rotation of the director triad. The skew-symmetry of $\boldsymbol{\eta}$ implies that the rigid director triad possesses only three independent rotational degrees of freedom.

It is emphasized that (A.1) is a *kinematic constraint*. Hence, the constrained theory discussed here is not obtained by a constitutive specialization (e.g., by setting $\ell = 0$), but by restricting the admissible director motions. This distinction is important when interpreting the reduction to classical continua.

To enforce the orthonormality constraints, the intrinsic director couples $\mathbf{t}^i$ are decomposed into constitutively determined and constraint-induced parts as

$$\mathbf{t}^i = \hat{\mathbf{t}}^i + \tilde{\mathbf{t}}^i, \qquad \tilde{\mathbf{t}}^i = \gamma^{ij}\mathbf{e}_j, \qquad \gamma^{ij} = \gamma^{ji}, \tag{A.2}$$

where $\hat{\mathbf{t}}^i$ are determined by the constitutive Eq. (23), with $\varepsilon_{\rm dir} = 0$:

$$\hat{\mathbf{t}}^i = -Gk_2(\boldsymbol{\psi}'^T - \boldsymbol{\eta}'^T). \tag{A.3}$$

In these expressions $\tilde{\mathbf{t}}^i$ represent the reactions associated with the orthonormality constraints. The quantities γ^{ij} are Lagrange multipliers that enforce the rigidity of the director triad and ensure that the constraint responses do no work i.e.,

$$\tilde{\mathbf{t}}^i \otimes \mathbf{e}_i = (\tilde{\mathbf{t}}^i \otimes \mathbf{e}_i)^T, \qquad (\tilde{\mathbf{t}}^i \otimes \mathbf{e}_i) \cdot \dot{\boldsymbol{\eta}}^T = 0. \tag{A.4}$$

Moreover, from (8), (21) and (A.1) it follows that

$$\chi^k_{ij} = 0, \qquad \mathbf{M}^i = \mathbf{0}, \tag{A.5}$$

which shows that the balances of director momentum (10) no longer involve higher-order spatial derivatives of $\boldsymbol{\eta}$ and can be rewritten in the tensorial form

$$\rho_z \mathbf{b}^i \otimes \mathbf{e}_i + Gk_2(\boldsymbol{\psi}'^T - \boldsymbol{\eta}'^T) - \gamma^{ij}\mathbf{e}_i \otimes \mathbf{e}_j - \rho_z y^{ij}\ddot{\mathbf{d}}_j \otimes \mathbf{e}_i = \mathbf{0}. \tag{A.6}$$

The symmetric part of this equation determines the Lagrange multipliers γ^{ij} whereas the skew-symmetric part governs the evolution of the three independent components of $\boldsymbol{\eta}$.

A key point is that the vanishing of χ^k_{ij} (and thus of $\mathbf{M}^i$) in the small-deformation constrained theory follows from (A.1) together with the specific definition of the curvature measures in the deformable Cosserat formulation. Therefore, even after imposing a rigid triad constraint, the resulting constrained model does not recover the rigid Cosserat theory, whose curvature energetics are instead driven by gradients of a rotation field. This distinction is further discussed below.

Next, it is of interest to note that in the absence of specific external director couples $\mathbf{b}^i$ and director inertia y^{ij} this balance of director momentum yields

$$\gamma^{ij}\mathbf{e}_i \otimes \mathbf{e}_j = \frac{1}{2}Gk_2(\boldsymbol{\psi}' + \boldsymbol{\psi}'^T), \quad \boldsymbol{\eta}' = \frac{1}{2}(\boldsymbol{\psi}' - \boldsymbol{\psi}'^T). \tag{A.7}$$

Thus, from (21) and (A.7) it follows that

$$\mathbf{T} = -p\mathbf{I} + G\big(\xi + \frac{k_2}{2}\big)(\boldsymbol{\psi}' + \boldsymbol{\psi}'^T), \tag{A.8}$$

which is a symmetric tensor with the effective shear modulus enhanced by the value of k_2. It follows that k_2 must vanish to model a Cauchy material.

This result also clarifies an important difference between the constrained and unconstrained theories. In the *unconstrained* deformable Cosserat model, setting $\ell = 0$ (in the absence of external director couples and director inertia) is sufficient to recover the classical Cauchy continuum, because the director contributions associated with $\mathbf{M}^i$ are switched off and no constraint reactions are present. In contrast, in the *constrained* theory the kinematic restriction (A.1) introduces the Lagrange multipliers γ^{ij} and the associated constraint reactions. Consequently, even if $\ell = 0$ (so that $\mathbf{M}^i = 0$), the Cauchy model is not recovered *within the present small-deformation constitutive setting* unless additional restrictions are imposed (in particular, $k_2 = 0$). In other words, the recovery

of the classical Cauchy continuum in the constrained theory depends on the combined effect of the kinematic constraint and of the constitutive choices, and is not controlled by ℓ alone.

To better understand why the director couple tensors $\mathbf{M}^i$ vanish in the small deformation equations with a constrained rigid director triad it is emphasized that the curvature measures χ^k_{ij} defined in the deformable Cosserat model [23] were formulated to ensure that χ^k_{ij} vanish whenever $\bar{\mathbf{m}}_i = \mathbf{d}_i$ are equal orthonormal triads, even when the orientation of these triads vary through the body. This implies that, χ^k_{ij} in Eq. (8) vanishes whenever $\boldsymbol{\eta}$ is skew-symmetric, independently of spatial variations in the orientation of the director triad. This feature allows the theory to describe, for example, curved fiber architectures in biological tissues in their zero-stress states. In contrast, the higher-order couple stress in the classical rigid Cosserat model is a linear function of the gradient $\varphi_{i,j}$ of a rotation vector φ_i (see Eq. (B.3)) that parameterizes the orientation of the rigid director triad. This means that this gradient must vanish in any zero-stress state of the rigid Cosserat model. As a consequence, even after imposing a rigid triad constraint, the resulting constrained model does not recover the *standard* rigid Cosserat theory, whose curvature energetics are instead driven by gradients of an independent rotation field. It is also noted that although the nonlinear theory admits non-vanishing higher-order stress contributions $\mathbf{M}^i$ under rigid director constraints, these contributions are nonlinear and vanish in the small-deformation limit considered in the present work.

Appendix B. Finite element formulation of the rigid Cosserat model

Following [13,14], the internal virtual power for a body occupying a region P, for the rigid Cosserat model is given by

$$\delta W_{\text{int}} = \int_P \left(\mathbf{T}_{\text{sym}} \cdot \delta \boldsymbol{\psi}_{\text{sym}} + \mathbf{T}_{\text{skw}} \cdot \delta \boldsymbol{\omega} + \boldsymbol{\mu} \cdot \delta \boldsymbol{\zeta} \right) \mathrm{d}V, \tag{B.1}$$

where $\boldsymbol{\mu}$ is the tensor of the microcouples, $\mathbf{T}_{\text{sym}}$ and $\mathbf{T}_{\text{skw}}$ are the symmetric and skew parts of the Cauchy stress $\mathbf{T}$ respectively, i.e., in tensorial notation,

$$\mathbf{T}_{\text{sym}} = \frac{1}{2}\left(\mathbf{T} + \mathbf{T}^T\right), \quad \mathbf{T}_{\text{skw}} = \frac{1}{2}\left(\mathbf{T} - \mathbf{T}^T\right), \tag{B.2}$$

the curvature $\boldsymbol{\zeta}$ is defined as a function of the rotation vector φ_i, such that

$$\zeta_{ij} = \varphi_{i,j}, \tag{B.3}$$

and

$$\omega_{ij} = \frac{1}{2}\left(\psi_{ji} - \psi_{ij}\right) + \epsilon_{ijk}\,\varphi_k, \tag{B.4}$$

represents the *relative* rotation of the material matrix with respect to that prescribed to the *micro-volumes* embedded at each material point $\mathbf{x}$ [14], and ϵ_{ijk} is the Levi-Civita permutation tensor. Hence, (B.1) can be rewritten as

$$\delta W_{\text{int}} = \int_P \left(T_{ij}\,\delta\psi_{ji} + \epsilon_{ijk}\left(\mathbf{T}_{\text{skw}}\right)_{ij}\,\delta\varphi_k + \mu_{ij}\,\delta\zeta_{ij} \right) \mathrm{d}V. \tag{B.5}$$

In the plane strain case, the DoFs reduce to three, that is, the two in-plane displacement components u_1 and u_2 and the out-of-plane component of the rotation vector φ_3. The skew-symmetric tensor $-\epsilon_{ijk}\,\delta\varphi_k$ can be discretized as a function of the nodal values of φ_3 as:

$$\varphi_3(\boldsymbol{r}) = \sum_{k=1}^{n_\varphi} N^{(k)}_\varphi(\boldsymbol{r})\hat{\varphi}^{(k)}_3, \tag{B.6}$$

where $n_\varphi \le n$ is the number of nodes in which φ_3 is discretized and $N^{(k)}_\varphi(\boldsymbol{r})$ is a standard polynomial shape function — that may be of different order with respect to $N^{(k)}(\boldsymbol{r})$ — referred to the kth node. Hence, the skew-symmetric tensor $(-\epsilon_{ijk}\,\delta\varphi_k)$ can be computed as:

$$-\epsilon_{ijk}\,\delta\varphi_k = \begin{bmatrix} 0 \\ 0 \\ 0 \\ -\varphi_3 \\ \varphi_3 \end{bmatrix} = \mathcal{M}(\mathbf{N}_\varphi)\delta\hat{\boldsymbol{\varphi}}, \tag{B.7}$$

where $\mathcal{M}(\mathbf{N}_\varphi)$ is a linear function that maps the components of the array of the shape functions $\mathbf{N}_\varphi$ into a $5 \times n_\varphi$ matrix. The non-vanishing components of the curvature tensor ζ_{ij} are stored in the array:

$$\boldsymbol{\zeta} = \begin{bmatrix} \varphi_{3,1} \\ \varphi_{3,2} \end{bmatrix}. \tag{B.8}$$

Hence, $\delta\boldsymbol{\zeta}$ can be discretized as a function of $\delta\hat{\boldsymbol{\varphi}}$ as:

$$\delta\boldsymbol{\zeta} = \mathcal{H}(\mathbf{H}_\varphi)\delta\hat{\boldsymbol{\varphi}}, \tag{B.9}$$

where the matrix $\mathbf{H}_\varphi$ contains the derivatives of the shape functions $\mathbf{N}_\varphi$ with respect to the reference coordinate system, that can be computed as

$$\mathbf{H} = \boldsymbol{J}^{-1}\mathbf{H}_{\varphi p}, \tag{B.10}$$

where $\mathbf{H}_{\varphi p}$, recorded in Appendix D, is the matrix containing the derivatives of $\mathbf{N}_{\varphi}$ with respect to $\boldsymbol{r}$, and $\mathcal{H}(\mathbf{H}_{\varphi})$ is a linear function that maps the components of $\mathbf{H}_{\varphi}$ into a $2 \times n_{\varphi}$ matrix. Under these assumptions, Eq. (B.5) can be discretized as

$$\delta W_{\text{int}} = \int_P \left[\delta\hat{\mathbf{u}}^T \mathcal{A}^T \mathbf{T} + \delta\hat{\boldsymbol{\varphi}}^T \left(\mathcal{H}^T \boldsymbol{\mu} - \mathcal{M}^T \mathbf{T}_{\text{skw}}\right)\right] \mathrm{d}V, \tag{B.11}$$

which, being valid for any kinematically admissible value of $\delta\hat{\mathbf{u}}, \delta\hat{\boldsymbol{\varphi}}$, gives the following internal forces

$$\mathbf{F}_u^{\text{int}} = \int_P \mathcal{A}^T \mathbf{T}\, \mathrm{d}V, \quad \mathbf{F}_{\varphi}^{\text{int}} = \int_P \left(\mathcal{H}^T \boldsymbol{\mu} - \mathcal{M}^T \mathbf{T}_{\text{skw}}\right) \mathrm{d}V. \tag{B.12}$$

The stresses can be computed as [13,14]

$$\begin{aligned} \mathbf{T} &= G\, \mathcal{I}_d \left[\xi(\mathcal{A} + \mathcal{T}\mathcal{A})\hat{\mathbf{u}}\right] + \left(k_v G\right)\mathbf{I}\left(\mathbf{I}^T \mathcal{A}\hat{\mathbf{u}}\right) + \mathbf{T}_{\text{skw}}, \\ \mathbf{T}_{\text{skw}} &= k_3\, G\left[(\mathcal{A} - \mathcal{T}\mathcal{A})\hat{\mathbf{u}} - 2\mathcal{M}\hat{\boldsymbol{\varphi}}\right], \\ \boldsymbol{\mu} &= \begin{bmatrix} \mu_{31} \\ \mu_{32} \end{bmatrix} = 2\, G\ell^2 \mathcal{H}\hat{\boldsymbol{\varphi}}, \end{aligned} \tag{B.13}$$

and the damage parameter ξ is computed as described in Section 2.6.

The FE stiffness matrix is obtained by differentiating the internal forces $\mathbf{F}_u^{\text{int}}$ and $\mathbf{F}_{\phi}^{\text{int}}$ with respect to the nodal displacements $\hat{\mathbf{u}}$ and the nodal tensor $\hat{\boldsymbol{\varphi}}$, i.e.,

$$\mathbf{K} = \begin{bmatrix} \mathbf{K}_{uu} & \mathbf{K}_{u\varphi} \\ \mathbf{K}_{\varphi u} & \mathbf{K}_{\varphi\varphi}, \end{bmatrix} \tag{B.14}$$

where:

$$\begin{aligned} \mathbf{K}_{uu} &= \frac{\partial \mathbf{F}_u^{\text{int}}}{\partial \hat{\mathbf{u}}} = \int_P G\, \mathcal{A}^T \left\{ \mathcal{I}_d \left[\xi(\mathcal{A} + \mathcal{T}\mathcal{A})\right] + k_v \mathbf{I}\left(\mathbf{I}^T \mathcal{A}\right) + k_3(\mathcal{A} - \mathcal{T}\mathcal{A}) + \mathcal{I}_d \left[(\mathcal{A} + \mathcal{T}\mathcal{A})\hat{\mathbf{u}}\right] \left(\frac{\mathrm{d}\xi}{\mathrm{d}\hat{\mathbf{u}}}\right)^T \right\} \mathrm{d}V, \\ \mathbf{K}_{u\varphi} &= \frac{\partial \mathbf{F}_u^{\text{int}}}{\partial \hat{\boldsymbol{\varphi}}} = \int_P -\left(2k_3\, G\right)\mathcal{A}^T \mathcal{M}\, \mathrm{d}V, \\ \mathbf{K}_{\varphi u} &= \frac{\partial \mathbf{F}_{\varphi}^{\text{int}}}{\partial \hat{\mathbf{u}}} = \int_P -\left(k_3\, G\right)\mathcal{M}^T (\mathcal{A} - \mathcal{T}\mathcal{A})\, \mathrm{d}V, \\ \mathbf{K}_{\varphi\varphi} &= \frac{\partial \mathbf{F}_{\varphi}^{\text{int}}}{\partial \hat{\boldsymbol{\varphi}}} = \int_P 2G\left[\ell^2 \mathcal{H}^T \mathcal{H} + k_3 \mathcal{M}^T \mathcal{M}\right] \mathrm{d}V. \end{aligned} \tag{B.15}$$

Appendix C. Finite Element operators for the plane strain formulation

The matrix $\mathbf{H}_p$ that contains the derivatives of the shape functions for displacements and geometry with respect to the intrinsic coordinate system $\boldsymbol{r}$, can be expressed as

$$\mathbf{H}_p = \begin{bmatrix} \frac{\partial N^{(1)}}{\partial r} & \cdot & \frac{\partial N^{(n)}}{\partial r} \\ \frac{\partial N^{(1)}}{\partial s} & \cdot & \frac{\partial N^{(n)}}{\partial s} \end{bmatrix}. \tag{C.1}$$

In the same way, the matrices $\mathbf{H}_{\eta p}$ and $\mathbf{H}_{\varphi p}$ that contain the derivatives of the shape functions for the tensor components η_{ij} and for the vector components φ_3 with respect to the intrinsic coordinate system $\boldsymbol{r}$, can be expressed as

$$\mathbf{H}_{\eta p} = \begin{bmatrix} \frac{\partial N_{\eta}^{(1)}}{\partial r} & \cdot & \frac{\partial N_{\eta}^{(n_\eta)}}{\partial r} \\ \frac{\partial N_{\eta}^{(1)}}{\partial s} & \cdot & \frac{\partial N_{\eta}^{(n_\eta)}}{\partial s} \end{bmatrix}, \quad \mathbf{H}_{\varphi p} = \begin{bmatrix} \frac{\partial N_{\varphi}^{(1)}}{\partial r} & \cdot & \frac{\partial N_{\varphi}^{(n_\varphi)}}{\partial r} \\ \frac{\partial N_{\varphi}^{(1)}}{\partial s} & \cdot & \frac{\partial N_{\varphi}^{(n_\varphi)}}{\partial s} \end{bmatrix}. \tag{C.2}$$

The jacobian, in the reference coordinate system, can be computed as

$$\boldsymbol{J} = \mathbf{H}_p \hat{\mathbf{X}}, \tag{C.3}$$

where

$$\hat{\mathbf{X}} = \begin{bmatrix} \hat{x}_1^{(1)} & \hat{x}_2^{(1)} \\ \cdot & \cdot \\ \hat{x}_1^{(n)} & \hat{x}_2^{(n)} \end{bmatrix}. \tag{C.4}$$

The nodal displacements are ordered in the vector $\hat{\mathbf{u}}$ of $2n$ components

$$\hat{\mathbf{u}} = \begin{bmatrix} \hat{u}_1^{(1)} & \hat{u}_2^{(1)} & \cdot & \hat{u}_1^{(n)} & \hat{u}_2^{(n)} \end{bmatrix}^T.$$

The components of the tensor η_{ij} at the nodes are stored in an array $\hat{\boldsymbol{\eta}}$ of $4n_\eta$ components

$$\hat{\boldsymbol{\eta}} = \left[\hat{\eta}_{11}^{(1)} \quad \hat{\eta}_{22}^{(1)} \quad \hat{\eta}_{12}^{(1)} \quad \hat{\eta}_{21}^{(1)} \quad . \quad \hat{\eta}_{11}^{(n_\eta)} \quad \hat{\eta}_{22}^{(n_\eta)} \quad \hat{\eta}_{12}^{(n_\eta)} \quad \hat{\eta}_{21}^{(n_\eta)}\right]^T. \tag{C.5}$$

The vector components φ_3 at the nodes are stored in an array of n_φ components

$$\hat{\boldsymbol{\varphi}} = \left[\hat{\varphi}_3^{(1)} \quad . \quad \hat{\varphi}_3^{(n_\varphi)}\right]^T.$$

The second-order identity tensor, in array notation, has the form

$$\mathbf{I} = \begin{bmatrix}1 & 1 & 1 & 0 & 0\end{bmatrix}^T, \tag{C.6}$$

while the operators $\mathcal{I}_d$ and $\mathcal{T}$, to compute the deviatoric part and the transpose of a second order tensor in 2D array notation, are respectively equal to:

$$\mathcal{I}_d = \begin{bmatrix} \frac{2}{3} & -\frac{1}{3} & -\frac{1}{3} & 0 & 0 \\ -\frac{1}{3} & \frac{2}{3} & -\frac{1}{3} & 0 & 0 \\ -\frac{1}{3} & -\frac{1}{3} & \frac{2}{3} & 0 & 0 \\ 0 & 0 & 0 & 1 & 0 \\ 0 & 0 & 0 & 0 & 1 \end{bmatrix}, \quad \mathcal{T} = \begin{bmatrix} 1 & 0 & 0 & 0 & 0 \\ 0 & 1 & 0 & 0 & 0 \\ 0 & 0 & 1 & 0 & 0 \\ 0 & 0 & 0 & 0 & 1 \\ 0 & 0 & 0 & 1 & 0 \end{bmatrix}. \tag{C.7}$$

The $\mathcal{A}(\mathbf{H})$ operator is a linear function that maps the components of $\mathbf{H}$ into the $5 \times 2n$ matrix and has the form

$$\mathcal{A}(\mathbf{H}) = \begin{bmatrix} (\mathbf{H})_{11} & 0 & . & (\mathbf{H})_{1n} & 0 \\ 0 & (\mathbf{H})_{21} & . & 0 & (\mathbf{H})_{2n} \\ 0 & 0 & . & 0 & 0 \\ (\mathbf{H})_{21} & 0 & . & (\mathbf{H})_{2n} & 0 \\ 0 & (\mathbf{H})_{11} & . & 0 & (\mathbf{H})_{1n} \end{bmatrix}. \tag{C.8}$$

The operator $\mathcal{N}(\mathbf{N}_\eta)$ is a linear function that maps the shape functions $\mathbf{N}_\eta$ into a $5 \times 4n_\eta$ matrix, which is defined by

$$\mathcal{N}(\mathbf{N}_\eta) = \begin{bmatrix} N_\eta^{(1)} & 0 & 0 & 0 & . & N_\eta^{(n_\eta)} & 0 & 0 & 0 \\ 0 & N_\eta^{(1)} & 0 & 0 & . & 0 & N_\eta^{(n_\eta)} & 0 & 0 \\ 0 & 0 & 0 & 0 & . & 0 & 0 & 0 & 0 \\ 0 & 0 & N_\eta^{(1)} & 0 & . & 0 & 0 & N_\eta^{(n_\eta)} & 0 \\ 0 & 0 & 0 & N_\eta^{(1)} & . & 0 & 0 & 0 & N_\eta^{(n_\eta)} \end{bmatrix}. \tag{C.9}$$

The operator $\mathcal{G}(\mathbf{H}_\eta)$ is a linear function that maps the components of $\mathbf{H}_\eta$ into a $8 \times 4n_\eta$ matrix, which is defined by

$$\mathcal{G}(\mathbf{H}_\eta) = \begin{bmatrix} (\mathbf{H}_\eta)_{11} & 0 & 0 & 0 & . & (\mathbf{H}_\eta)_{1n_\eta} & 0 & 0 & 0 \\ 0 & (\mathbf{H}_\eta)_{11} & 0 & 0 & . & 0 & (\mathbf{H}_\eta)_{1n_\eta} & 0 & 0 \\ 0 & 0 & (\mathbf{H}_\eta)_{11} & 0 & . & 0 & 0 & (\mathbf{H}_\eta)_{1n_\eta} & 0 \\ 0 & 0 & 0 & (\mathbf{H}_\eta)_{11} & . & 0 & 0 & 0 & (\mathbf{H}_\eta)_{1n_\eta} \\ (\mathbf{H}_\eta)_{21} & 0 & 0 & 0 & . & (\mathbf{H}_\eta)_{2n_\eta} & 0 & 0 & 0 \\ 0 & (\mathbf{H}_\eta)_{21} & 0 & 0 & . & 0 & (\mathbf{H}_\eta)_{2n_\eta} & 0 & 0 \\ 0 & 0 & (\mathbf{H}_\eta)_{21} & 0 & . & 0 & 0 & (\mathbf{H}_\eta)_{2n_\eta} & 0 \\ 0 & 0 & 0 & (\mathbf{H})_{21} & . & 0 & 0 & 0 & (\mathbf{H}_\eta)_{2n_\eta} \end{bmatrix} \tag{C.10}$$

The operator $\mathcal{G}_\mathcal{T}(\mathbf{H}_\eta)$ is a linear function that maps the components of $\mathbf{H}_\eta$ into a $8 \times 4n_\eta$ matrix, which is defined by

$$\mathcal{G}_\mathcal{T}(\mathbf{H}_\eta) = \begin{bmatrix} (\mathbf{H}_\eta)_{11} & 0 & 0 & 0 & . & (\mathbf{H}_\eta)_{1n_\eta} & 0 & 0 & 0 \\ 0 & (\mathbf{H}_\eta)_{11} & 0 & 0 & . & 0 & (\mathbf{H}_\eta)_{1n_\eta} & 0 & 0 \\ 0 & 0 & 0 & (\mathbf{H}_\eta)_{11} & . & 0 & 0 & 0 & (\mathbf{H}_\eta)_{1n_\eta} \\ 0 & 0 & (\mathbf{H}_\eta)_{11} & 0 & . & 0 & 0 & (\mathbf{H}_\eta)_{1n_\eta} & 0 \\ (\mathbf{H}_\eta)_{21} & 0 & 0 & 0 & . & (\mathbf{H}_\eta)_{2n_\eta} & 0 & 0 & 0 \\ 0 & (\mathbf{H}_\eta)_{21} & 0 & 0 & . & 0 & (\mathbf{H}_\eta)_{2n_\eta} & 0 & 0 \\ 0 & 0 & 0 & (\mathbf{H})_{21} & . & 0 & 0 & 0 & (\mathbf{H}_\eta)_{2n_\eta} \\ 0 & 0 & (\mathbf{H}_\eta)_{21} & 0 & . & 0 & 0 & (\mathbf{H}_\eta)_{2n_\eta} & 0 \end{bmatrix}, \tag{C.11}$$

where $\mathcal{M}(\mathbf{N}_\varphi)$ is a linear function that maps the components of the shape functions $\mathbf{N}_\varphi$ into a $5 \times n_\varphi$ matrix, which is defined by

$$\mathcal{M}(\mathbf{N}_\varphi) = \begin{bmatrix} 0 & . & 0 \\ 0 & . & 0 \\ 0 & . & 0 \\ -N_\varphi^{(1)} & . & -N_\varphi^{(n_\varphi)} \\ N_\varphi^{(1)} & . & N_\varphi^{(n_\varphi)} \end{bmatrix}. \tag{C.12}$$

Finally, $\mathcal{H}(\mathbf{H}_\varphi)$ is a linear function that maps the components of $\mathbf{H}_\varphi$ into a $2\times n_\varphi$ matrix, which is defined by

$$\mathcal{H}(\mathbf{H}_\varphi)=\mathbf{H}_\varphi. \tag{C.13}$$

Appendix D. Plane strain shear: Analytical solution

Using the kinematics (44) for plane strain shear and the constitutive Eq. (23) the non-zero kinetic quantities are given by

$$\begin{aligned} &T_{12}=G\left[\left(1+k_2\right)\frac{\mathrm{d}u_1}{\mathrm{d}x_2}-k_2\eta_{21}\right], \quad T_{21}=G\frac{\mathrm{d}u_1}{\mathrm{d}x_2},\\ &t^1_2=-k_2\,G\left(\frac{\mathrm{d}u_1}{\mathrm{d}x_2}-\eta_{21}\right) \qquad\qquad t^2_1=0,\\ &M^1_{22}=M^2_{12}=2G\ell^2\frac{\mathrm{d}\eta_{21}}{\mathrm{d}x_2}. \end{aligned} \tag{D.1}$$

In the absence of inertia, body force b_i and all components of the external assigned director couples except b^2_1, the equilibrium Eq. (25) require

$$\frac{\mathrm{d}T_{12}}{\mathrm{d}x_2}=0, \quad \rho_z b^1_2=t^1_2-\frac{\mathrm{d}M^1_{22}}{\mathrm{d}x_2}, \quad \frac{\mathrm{d}M^2_{12}}{\mathrm{d}x_2}=0, \tag{D.2}$$

the second of which determines the assigned director couple b^2_1. Next, using the constitutive Eq. (D.1) these equations can be written in the forms

$$\left(1+k_2\right)\frac{\mathrm{d}^2u_1}{\mathrm{d}x_2^2}-k_2\frac{\mathrm{d}\eta_{21}}{\mathrm{d}x_2}=0, \quad \frac{\mathrm{d}^2\eta_{21}}{\mathrm{d}x_2^2}=0. \tag{D.3}$$

Then, the boundary conditions (43) at the bottom and top of the strip are given by

$$u_1(0)=0, \quad u_1(H)=\bar{u}, \quad \eta_{21}(0)=0, \quad \eta_{21}(H)=\bar{\eta}, \tag{D.4}$$

and the solutions are given by

$$\begin{aligned} &u_1=\frac{\bar{u}}{H}x_2-\frac{k_2\bar{\eta}}{2(1+k_2)}x_2\left(1-\frac{x_2}{H}\right), \quad \eta_{21}=\frac{\bar{\eta}}{H}x_2,\\ &\frac{T_{12}}{G}=(1+k_2)\frac{\bar{u}}{H}-\frac{k_2}{2}\bar{\eta}, \quad \frac{T_{21}}{G}=\frac{\bar{u}}{H}+\frac{k_2\bar{\eta}}{1+k_2}\left(\frac{x_2}{H}-\frac{1}{2}\right),\\ &\frac{M^1_{22}}{GH}=\frac{M^2_{12}}{GH}=2\left(\frac{\ell}{H}\right)^2\bar{\eta}. \end{aligned} \tag{D.5}$$

References

[1] E.M.P. Cosserat, F. Cosserat, Théorie des corps déformables. A. Hermann et fils, 1909.
[2] A.C. Eringen, E. Suhubi, Nonlinear theory of simple micro-elastic solids-I, Int. J. Eng. Sci 2 (1964) 189–203. https://doi.org/10.1016/0020-7225(64)90004-7
[3] E. Suhubi, A.C. Eringen, Nonlinear theory of micro-elastic solids-II, Int. J. Eng. Sci 2 (1964) 389–404. https://doi.org/10.1016/0020-7225(64)90017-5
[4] S. Forest, Micromorphic approach to materials with internal length, in: Encyclopedia of Continuum Mechanics, Springer, 2020, pp. 1643–1652. https://doi.org/10.1007/978-3-662-53605-6_150-1
[5] P. Germain, The method of virtual power in continuum mechanics. Part 2: microstructure, SIAM J. Appl. Math 25 (1973) 556–575. https://doi.org/10.1137/0125053
[6] R.D. Mindlin, Micro-structure in linear elasticity, Arch. Ration. Mech. Anal 16 (1964) 51–78. https://doi.org/10.1007/BF00248490
[7] R.D. Mindlin, Second gradient of strain and surface-tension in linear elasticity, Int. J. Solids Struct 1 (1965) 417–438. https://doi.org/10.1016/0020-7683(65)90006-5
[8] R.D. Mindlin, H. Tiersten, Effects of couple-stresses in linear elasticity, Arch. Ration. Mech. Anal 11 (1962) 415–448. https://doi.org/10.1007/BF00253946
[9] A.E. Green, R.S. Rivlin, Multipolar continuum mechanics. Arch. Ration. Mech. Anal 17 (1964) 113–147. https://doi.org/10.1007/BF00253051
[10] C. Truesdell, R. Toupin, The Classical Field Theories. Handbuch der Physik III/1, Springer, Berlin, 1960. https://doi.org/10.1007/978-3-642-45943-6_2
[11] R. De Borst, Simulation of strain localization: a reappraisal of the Cosserat continuum, Eng. Comput 8 (1991) 317–332. https://doi.org/10.1108/eb023842
[12] H.B. Mühlhaus, I. Vardoulakis, The thickness of shear bands in granular materials, Geotechnique 37 (1987) 271–283. https://doi.org/10.1680/geot.1987.37.3.271
[13] A. Panteghini, R. Lagioia, An implicit integration algorithm based on invariants for isotropic elasto-plastic models of the Cosserat continuum, Int. J. Numer. Anal. Met 46 (2022a) 2233–2267. https://doi.org/10.1002/nag.3386
[14] A. Panteghini, R. Lagioia, A micropolar isotropic plasticity formulation for non-associated flow rule and softening featuring multiple classical yield criteria, Int. J. Numer. Anal. Met 46 (2022) 674–696. https://doi.org/10.1002/nag.3316
[15] D. Perić, J. Yu, D. Owen, On error estimates and adaptivity in elastoplastic solids: applications to the numerical simulation of strain localization in classical and Cosserat continua, Int. J. Num. Meth. Eng 37 (1994) 1351–1379. https://doi.org/10.1002/nme.1620370806
[16] I. Vardoulakis, Cosserat continuum mechanics, Lecture Notes in Applied and Computational Mechanics 87 (2019). https://doi.org/10.1007/978-3-319-95156-0
[17] A. Khoei, K. Karimi, An enriched-fem model for simulation of localization phenomenon in Cosserat continuum theory, Comput. Mater. Sci 44 (2008) 733–749. https://doi.org/10.1016/j.commatsci.2008.05.019
[18] A. Khoei, S. Yadegari, S. Biabanaki, 3D finite element modeling of shear band localization via the micro-polar Cosserat continuum theory, Comput. Mater. Sci 49 (2010) 720–733. https://doi.org/10.1016/j.commatsci.2010.06.015
[19] E. Sharbati, R. Naghdabadi, Computational aspects of the Cosserat finite element analysis of localization phenomena, Comput. Mater. Sci 38 (2006) 303–315. https://doi.org/10.1016/j.commatsci.2006.03.003

[20] S.A. Sabet, R. De Borst, Mesh bias and shear band inclination in standard and non-standard continua, Arch. Appl. Mech 89 (2019) 2577–2590. https://doi.org/10.1007/s00419-019-01593-2
[21] G. Russo, S. Forest, C. Girot-Mata, Thermomechanics of Cosserat media: modeling adiabatic shear bands in metals, Continuum Mech. Therm 32 (2020) 1051–1076. https://doi.org/10.1007/s00161-020-00930-z
[22] H. Ebrahimian, S. Pietruszczak, I. Vardoulakis, Modeling shear localization along granular soil-structure interfaces using elasto-plastic Cosserat continuum, Int. J. Solids Struct 49 (2012) 2797–2809. https://doi.org/10.1016/j.ijsolstr.2011.09.005
[23] M.B. Rubin, A thermomechanical Eulerian formulation of a size-dependent elastic-inelastic Cosserat continuum, J. Elast 157 (2025) 12. https://doi.org/10.1007/s10659-024-10105-5
[24] M.B. Rubin, Correction to "A thermomechanical eulerian formulation of a size-dependent elastic-inelastic cosserat continuum, J Elast 157, 77 (2025b). https://doi.org/10.1007/s10659-025-10173-1
[25] S.S. Antman, The theory of rods, in: S. Flugge's Handbuch der Physik, 1972, pp. 641–703. https://doi.org/10.1007/978-3-662-39776-3_6
[26] A.E. Green, P. Naghdi, M. Wenner, On the theory of rods. i. derivations from the three-dimensional equations, Proc. R. Soc. A 337 (1974) 451–483. https://doi.org/10.1098/rspa.1974.0061
[27] A.E. Green, P. Naghdi, M. Wenner, On the theory of rods ii. developments by direct approach, Proc. R. Soc. A 337 (1974b) 485–507. https://doi.org/10.1098/rspa.1974.0062
[28] B. Nadler, M.B. Rubin, A new 3-D finite element for nonlinear elasticity using the theory of a Cosserat point, Int. J. Solids Struct 40 (2003) 4585–4614. https://doi.org/10.1016/S0020-7683(03)00210-5
[29] P.M. Naghdi, The theory of plates and shells, in: S. Flugge's Handbuch der Physik, 1972, pp. 425–640. https://doi.org/10.1007/978-3-662-39776-3_5
[30] M.B. Rubin, Cosserat theories: Shells, rods and points, 79, Springer Science & Business Media, 2000. https://doi.org/10.1007/978-94-015-9379-3
[31] E.T. Onat, The notion of state and its implications in thermodynamics of inelastic solids, in: Irreversible Aspects of Continuum Mechanics and Transfer of Physical Characteristics in Moving Fluids: Symposia Vienna, Springer, 1966, pp. 292–314. https://doi.org/10.1007/978-3-7091-5581-3_19
[32] M.B. Rubin, Removal of unphysical arbitrariness in constitutive equations for elastically anisotropic nonlinear elastic-viscoplastic solids, Int. J. Eng. Sci 53 (2012) 38–45. https://doi.org/10.1016/j.ijengsci.2011.12.008
[33] M.B. Rubin, Continuum Mechanics with Eulerian Formulations of Constitutive Equations, Springer Nature, 2021. https://doi.org/10.1007/978-3-030-57776-6
[34] L. Anand, Fracture of rock-like materials: a gradient-damage theory, Int. J. Solids Struct 325 (2026) 113739. https://doi.org/10.1016/j.ijsolstr.2025.113739
[35] M. Jirásek, Comparison of integral-type nonlocal plasticity models for strain-softening materials, Int. J. Eng. Sci 41 (2003) 1553–1602. https://doi.org/10.1016/S0020-7225(03)00027-2
[36] E. Lorentz, Gradient damage models: toward full-scale computations, Comput. Method. Appl. M 200 (2011) 90–109. https://doi.org/10.1016/j.cma.2010.07.015
[37] R.H.J. Peerlings, R. De Borst, W.A.M. Brekelmans, J.H.P. De Vree, Gradient enhanced damage for quasi-brittle materials, Int. J. Num. Meth. Eng 39 (1996) 3391–3403. https://doi.org/10.1002/(SICI)1097-0207(19961015)39:19<3391::AID-NME7>3.0.CO;2-D
[38] R.H.J. Peerlings, R. De Borst, W.A.M. Brekelmans, J.H.P. De Vree, Gradient-enhanced damage modelling of concrete fracture, Eng. Fract. Mech 60 (1998) 1–12. https://doi.org/10.1016/S0013-7944(97)00117-9
[39] A. Needleman, V. Tvergaard, Analyses of plastic flow localization in metals, Appl. Mech. Rev 45 (1992) S3–S18. https://doi.org/10.1115/1.3121390
[40] Z.P. Bažant, G. Pijaudier-Cabot, Nonlocal continuum damage, localization instability and convergence, J. Appl. Mech 55 (1988) 287–293. https://doi.org/10.1115/1.3173674
[41] Z.P. Bažant, M. Jirásek, Nonlocal integral formulations of plasticity and damage: survey of progress, J. Eng. Mech 128 (2002) 1119–1149. https://doi.org/10.1061/(ASCE)0733-9399(2002)128:11(1119)
[42] F.P. Duda, A. Ciarbonetti, P.J. Sánchez, A.E. Huespe, A phase-field/gradient damage model for brittle fracture in elastic-plastic solids, Int. J. Plasticity 65 (2015) 269–296. https://doi.org/10.1016/j.ijplas.2014.09.005
[43] C. Miehe, M. Hofacker, F. Welschinger, A phase field model for rate-independent crack propagation: robust algorithmic implementation based on operator splits, Comput. Method. Appl. M 199 (2010a) 2765–2778. https://doi.org/10.1016/j.cma.2010.01.008
[44] C. Miehe, F. Welschinger, M. Hofacker, Thermodynamically consistent phase-field models of fracture in elastic solids, Int. J. Num. Meth. Eng 83 (2010) 1273–1311. https://doi.org/10.1002/nme.2861
[45] C. Miehe, F. Aldakheel, S. Teichtmeister, Phase-field modeling of ductile fracture at finite strains: a robust variational-based numerical implementation of a gradient-extended theory by micromorphic regularization, Int. J. Num. Meth. Eng 111 (2017) 816–863. https://doi.org/10.1002/nme.5484
[46] M. Abatour, S. Forest, Strain gradient plasticity based on saturating variables, Eur. J. Mech. A-Solid 104 (2024) 105016. https://doi.org/10.1016/j.euromechsol.2023.105016
[47] J. Friedlein, J. Mergheim, P. Steinmann, Efficient gradient enhancements for plasticity with ductile damage in the logarithmic strain space, Eur. J. Mech. A-Solid 99 (2023). https://doi.org/10.1016/j.euromechsol.2023.104946
[48] G. Bacquaert, J. Bleyer, C. Maurini, Regularization of softening plasticity with the cumulative plastic strain-rate gradient, J. Mech. Phys. Solids 194 (2025) 105923. https://doi.org/10.1016/j.jmps.2024.105923
[49] S. Forest, Micromorphic approach for gradient elasticity, viscoplasticity, and damage, J. Eng. Mech 135 (2009) 117–131. https://doi.org/10.1061/(ASCE)0733-9399(2009)135:3(117)
[50] K. Langenfeld, J. Mosler, A micromorphic approach for gradient-enhanced anisotropic ductile damage, Comput. Method. Appl. M 360 (2020) 112717. https://doi.org/10.1016/j.cma.2019.112717
[51] L. Sobisch, T. Kaiser, A. Menzel, The non-stationary micromorphic approach to gradient-damage: on time and length scales, stable time increments and micromorphic damping, Comput. Method. Appl. M 448 (2026) 118478. https://doi.org/10.1016/j.cma.2025.118478
[52] P. Steinmann, A micropolar theory of finite deformation and finite rotation multiplicative elastoplasticity, Int. J. Solids Struct 31 (1994) 1063–1084. https://doi.org/10.1016/0020-7683(94)90164-3
[53] P. Steinmann, Theory and numerics of ductile micropolar elastoplastic damage, Int. J. Num. Meth. Eng 38 (1995) 583–606. https://doi.org/10.1002/nme.1620380406
[54] N. Aravas, S. Xenos, "Implicit" vs "Explicit" gradient plasticity models: do they always remove mesh dependence in softening materials?, Int. J. Solids Struct 281 (2023) 112415. https://doi.org/10.1016/j.ijsolstr.2023.112415
[55] L. Guo, X. Li, D. Song, J. Chen, Cosserat constitutive theory and one of its higher-order forms: a rediscussion on the mesh dependence problem, Finite Elem. Anal. Des 241 (2024) 104224. https://doi.org/10.1016/j.finel.2024.104224
[56] H. Tang, W. Wei, F. Liu, G. Chen, Elastoplastic Cosserat continuum model considering strength anisotropy and its application to the analysis of slope stability, Comput. Geotech 117 (2020) 103235. https://doi.org/10.1016/j.compgeo.2019.103235
[57] R. De Borst, S.A. Sabet, T. Hageman, Non-associated Cosserat plasticity, Int. J. Mech. Sci 230 (2022) 107535. https://doi.org/10.1016/j.ijmecsci.2022.107535
[58] J. Tejchman, Effect of fluctuation of current void ratio on the shear zone formation in granular bodies within micro-polar hypoplasticity, Comput. Geotech 33 (2006) 29–46. https://doi.org/10.1016/j.compgeo.2006.01.001
[59] T. Duretz, L. Räss, R. De Borst, T. Hageman, A comparison of plasticity regularization approaches for geodynamic modeling, Geochem. Geophys. Geosyst 24 (2023). https://doi.org/10.1029/2022GC010675
[60] D. Systèmes, ABAQUS User's & Theory Manuals - Release 6.24, Providence, RI, USA, 2024.